



The Origin and Composition of Saturn's Ring Moons

Mauro Ciarniello¹ · Gianrico Filacchione¹ · Philip D. Nicholson² ·
Matthew M. Hedman³ · Sebastien Charnoz⁴ · Jeffrey N. Cuzzi⁵ ·
Maryame El Moutamid⁶ · Amanda R. Hendrix⁷ · Nicolas Rambaux⁸ · Kelly E. Miller⁹ ·
Olivier Mousis^{10,11} · Kevin Baillie⁸ · Paul R. Estrada⁵ · J. Hunter Waite⁹

Received: 2 October 2023 / Accepted: 20 August 2024
© The Author(s) 2024

Abstract

Here we review the origin, evolution, and compositional properties of Saturn's ring moons. This class of eleven small satellites includes objects orbiting near the outer edge of the main rings (Pan, Daphnis, Atlas, Prometheus, Pandora, Janus, Epimetheus) and “ring-embedded” moons (Aegeon, Methone, Anthe, Pallene) orbiting inward of Enceladus and associated with either diffuse or partial rings. We discuss current formation scenarios, according to which ring moons could originate either in the main rings from accretion onto original seeds denser than the ring material, or outside the A ring from spontaneous accretion of ring particles, and then evolve outwards due to gravitational torque from the rings. Remote sensing observations of the ring moons from the Cassini mission are analyzed in the broader context of Saturn's icy moons and main rings observations. Spectroscopic data support a compositional paradigm similar to the main rings, dominated by water ice, and smaller amounts of two separate contaminants, in the form of a UV absorber and a spectrally neutral darkening material. Global radial trends in the spectral properties of the ring moons suggest that the surface composition is significantly affected by a complex interplay of exogenous processes, among which the contamination from nearby A ring particles, meteoritic bombardment, charged particle flux, and E ring particle accumulation, depending on the corresponding magnitude at the ring moon orbital distance and exposure time. These processes modify the original composition inherited by the rings and, coupled with the fact that the surface composition is likely representative only of the ring moon outer layers, make it difficult to trace back the present composition to a given ring moon formation scenario.

Keywords Ring moons · Composition · Origins · Surfaces · Ices · Saturn

1 Introduction

Among Saturn's 146 known satellites, as of 2023 (Sheppard et al. 2023), are eleven small inner satellites that are dynamically-related to the rings and which we refer to here as “ring moons”. Ring moons play a crucial role in preserving the rings from viscous expansion, a result of the collisions among ring particles which causes their diffusion through viscous interactions (Charnoz et al. 2009). Orbiting near the outer edge of the rings, ring moons are at the right distances from Saturn to generate strong orbital resonances, which, in addition

Extended author information available on the last page of the article

to the gravitational influence of the larger Mimas, are capable of restraining the ring viscous radial spreading (Lissauer and Cuzzi 1982; Tiscareno et al. 2007; Tajeddine et al. 2017a). The ‘dynamical age’ of the rings is thus closely linked to the presence, number and size of its associated ring moons (as well as Mimas), while being fundamentally driven by viscous spreading due to internal collisional interactions (Salmon et al. 2010).

The histories of Saturn’s ring moons and the ring system are strongly related among them since they probably share at least aspects of their origin. Numerical simulations show that collisions among ring particles can clump them together to form larger “dynamical ephemeral bodies”, up to tens of meters in size, which then undergo tidal disruption (Weidenschilling et al. 1984; Davis et al. 1984). However, if the accretion of ring material occurs onto a seed with density larger than that of ring particles, the aggregate can survive disruption to form a small moon (Charnoz et al. 2007, 2009). As a consequence, many of the ring moons could be the result of a recent aggregation of ring particles, that successively evolved outside the main ring system. Alternatively, spontaneous accretion of ring material might lead to the in situ formation of moons, if occurring at distances where the moonlet self-gravity overcomes local Saturn’s tidal forces. As a result of these formation processes, the ring moons preserve to some extent the composition of the ring particles from which were accreted, and can be considered as a “bridge” between the main rings and mid-sized icy satellites. Nonetheless, ring moon surfaces are also affected by a complex interplay of exogenous processes, such as contamination of nearby ring material (Buratti et al. 2019; Hedman et al. 2020), bombardment from magnetospheric particles (Roussos et al. 2008; Paranicas et al. 2018; Hedman et al. 2020), and contamination from meteoritic dust (Cuzzi et al. 2009), which modifies the physical and compositional properties of the material inherited from the main rings.

In this article we discuss the ring moon formation processes and investigate the surface composition of the ring moons in comparison to the main rings and the mid-sized icy satellites. This would help to improve our understanding of the processes determining the evolution of the Saturn’s system in general, and, by consequence, of the main rings, in an effort of finally constraining their primordial composition, origin and age.

We proceed by first introducing the different ring moon dynamical families (Sect. 2), then we summarize their structural and morphological properties (Sects. 3 and 4) and review current ring moon formation and orbital evolution scenarios (Sect. 5); the current understanding of the ring moon surface composition from Cassini remote sensing data, in comparison to Saturn’s ring and mid-sized icy satellites, is presented in Sect. 6 and it is complemented by a review of the composition of the F and G rings in Sect. 7; the exogenic processes affecting ring moon surface properties are addressed in Sect. 8; finally, in Sect. 9 we summarize the main findings and discuss the implications of the observed ring moon composition in the context of Saturn’s ring moon origin and evolution.

2 Ring Moon Dynamical Families

Following Thomas et al. (2013, 2018b), we may conveniently divide the ring moons into three families, based on their distinct orbital or dynamical environments:

- The inner ring moons, Pan, Daphnis, Atlas, Prometheus and Pandora, occupy orbits either within gaps in the rings (Pan and Daphnis), in close proximity to the A ring (Atlas), or straddling the narrow F ring (Prometheus and Pandora).
- The coorbital satellites, Janus and Epimetheus, share a common orbit located between the F ring and Mimas, exchanging their relative positions every 4 yrs.

- Aegaeon, Methone, Anthe and Pallene are all embedded within either narrow diffuse rings or partial rings/arcs. Aegaeon orbits within the G ring, located between the coorbitals and Mimas, while the other three occupy orbits between those of Mimas and Enceladus. Along with tiny Polydeuces, they are the smallest of the inner Saturnian moons.

In addition, there are four objects, Telesto, Calypso, Helene and Polydeuces that are not strictly-speaking 'ring moons', but small bodies that librate around the L_4 and L_5 triangular Lagrange points of the mid-sized satellites Tethys and Dione, respectively. These objects are probably most like the objects in the last group because they orbit within the E ring like Anthe, Methone and Pallene. Furthermore, just as the orbits of these moons are strongly perturbed by Tethys and Dione, the orbits of Aegaeon, Anthe and Methone are heavily influenced by mean-motion resonances with Mimas. The dynamical state and history of all these moons are therefore strongly influenced by Saturn's mid-sized satellites.

The ring moons' principal orbital characteristics are summarized in Table 1, based largely on fits to Voyager and Cassini optical navigation data by Spitale et al. (2006), Jacobson et al. (2008), Hedman et al. (2009, 2010), and Cooper et al. (2008, 2015). Most of these objects suffer significant orbital perturbations due to interactions with other satellites and the values listed in Table 1 are decade-long averages based on numerical integrations.

2.1 Inner Ring Moons

Pan is responsible for clearing and maintaining the 322 km-wide Encke gap in the outer A ring, at whose edges and in the adjoining ring material it drives a complex pattern of km-scale oscillations collectively referred to as 'satellite wakes' (Showalter et al. 1986; Weiss et al. 2009), from which its mass has been estimated.

Daphnis plays a similar role in the 35 km-wide Keeler gap, but is significantly smaller than Pan. It too drives oscillatory perturbations on the gap edges, from which its mass has been estimated (Weiss et al. 2009). Cassini observations have revealed occasional and irregular changes in its semimajor axis and orbital period, of unknown origin (Jacobson 2014; Santana et al. 2019).

Orbiting about 900 km outside the edge of the A ring, Atlas is similar to Pan in size and shape. Their non-spherical shapes could be the result of either accretion of ring particles (Charnoz et al. 2007) or the result of low-velocity collisions (Leleu et al. 2018).

Atlas orbit is mildly chaotic, apparently due to overlapping 54:43 mean-motion resonances (henceforth MMRs) with Prometheus (Cooper et al. 2015; Renner et al. 2016). Despite the initial assumption that probably inspired its name, Atlas does not 'hold up' the edge of the A ring. This task is instead currently largely accomplished by the 7:6 mean-motion resonance with Janus (Spitale and Porco 2009; Tajeddine et al. 2017a; Nicholson et al. 2018).

About 3400 km beyond the outer edge of the A ring lies the narrow, multi-stranded F ring, on either side of which orbit the satellites Prometheus and Pandora. Initially referred to as 'shepherd satellites', due to their perceived role in confining the F ring, subsequent studies have shown that the true situation is more complex, although many of the unusual periodic structures seen in this ring have been shown to be due to perturbations by Prometheus (Murray and Giuliatti Winter 1996; Murray et al. 2005). For a more detailed discussion of the F ring's structure and dynamics, the reader is referred to the reviews by Colwell et al. (2009) and Murray and French (2018). Observations of Prometheus and Pandora with HST in the mid-1990s, and some models, suggested that their orbits are chaotic, with discontinuities in their mean motions associated with the times — every 6.2 yrs — when the apocenter of the former was aligned with the pericenter of the latter (Poulet and Sicardy 2001; French et al.

Table 1 Orbital data for Saturn's ring moons¹. The JPL Horizons ID (Code), average semi-major axis (a_{mean}), eccentricity (Ecc.), inclination (Incl.) and period are reported for each target. For reference, also significant ring features are included, for which the corresponding radius (Rad.) is indicated. All moons outside Janus orbit within the diffuse E ring

Satellite/Ring	Code	a_{mean} /Rad. (km)	Ecc.	Incl. (deg)	Period (days)	Source
A ring inner edge		122,050				French et al. (2017)
Encke gap inner edge		133,423				French et al. (2017)
Pan ²	618	133,584	0.00001	0.0	0.575051	Jacobson et al. (2008)
Encke gap outer edge		133,745				French et al. (2017)
Keeler gap inner edge		136,487				Tajeddine et al. (2017b)
Daphnis ²	635	136,506	0.00003	0.004	0.594080	Jacobson et al. (2008)
Keeler gap outer edge		136,522				French et al. (2017)
A ring outer edge		136,770				El Moutamid et al. (2016)
Atlas	615	137,666	0.00116	0.003	0.601693	Cooper et al. (2015)
Prometheus ³	616	139,378	0.00223	0.008	0.612990	Cooper et al. (2015)
F ring core		140,221				Cuzzi et al. (2018a)
Pandora ³	617	141,712	0.00419	0.050	0.628503	Cooper et al. (2015)
Janus(a) ⁴	610	151,462	0.0068	0.164	0.694661	Cooper et al. (2015)
Janus(b) ⁴	610	151,441	0.0068	0.164	0.694517	Cooper et al. (2015)
Epimetheus(a) ⁴	611	151,414	0.0097	0.352	0.694329	Cooper et al. (2015)
Epimetheus(b) ⁴	611	151,489	0.0097	0.352	0.694850	Cooper et al. (2015)
Aegaeon ⁵	653	167,494	0.00024	0.001	0.808111	Hedman et al. (2010)
Methone ⁵	632	194,230	0.0000	0.013	1.009575	Jacobson et al. (2008)
Anthe ⁵	649	197,655	0.0012	0.017	1.036517	Cooper et al. (2008)
Pallene ⁵	633	212,280	0.0040	0.181	1.153746	Jacobson et al. (2008)
Telesto ⁶	613	~ 294,670	0.001	1.18	1.88780	SAT441
Calypso ⁶	614	~ 294,670	0.001	1.50	1.88780	SAT441
Helene ⁷	612	~ 377,410	0.007	0.21	2.73691	SAT441
Polydeuces ⁷	634	~ 377,410	0.019	0.18	2.73691	SAT441

¹Geometric elements fitted to the numerically-integrated orbit, or average epicyclic elements

²Pan & Daphnis are modeled as precessing ellipses

³Prometheus and Pandora interact chaotically at intervals of ~ 6.2 yrs when their pericenters are in anti-alignment

⁴Janus & Epimetheus share a common mean orbit, exchanging their relative positions every 4.0 yrs. Orbit (a) refers to the periods 2002-5 and 2010-3, while orbit (b) refers to the periods 2006-9 and 2014-7

⁵Aegaeon, Methone, Anthe, and Pallene orbit within faint dusty rings (see text)

⁶Telesto & Calypso librate about the L_4 and L_5 points of Tethys, respectively

⁷Helene & Polydeuces librate about the L_4 and L_5 points of Dione, respectively

2003). The chaos was later confirmed numerically but shown to be due to a series of overlapping 121:118 MMRs between the two moons (Goldreich and Rappaport 2003; Cooper et al. 2015). The dusty F ring itself lies in a dynamically chaotic region, but is anchored by a more massive large-particle core composed of multiple short arcs lying in locally-stable sites of a Corotation-Eccentricity resonance with Prometheus (Cuzzi 2024; Cuzzi et al. 2024). Nev-

ertheless, important questions (such as its uniqueness) remain unresolved. Its mass is very uncertain, though probably much less than that of Prometheus or Pandora, and collisional events observed by Cassini suggest that it contains many small moonlets embedded within the icy dust that dominates its visual appearance (Charnoz et al. 2005; Beurle et al. 2010; Attree et al. 2012; Murray and French 2018).

2.2 Coorbital Moons

Approximately 11,000 km beyond the F ring we find the co-orbital satellites, Janus and Epimetheus, the only known example in the Solar System of a pair of similar-mass objects trapped in a horseshoe libration about their mutual L_4 and L_5 Lagrange points (Dermott and Murray 1981). Every 4.0 years, the two moons suffer a close approach and exchange angular momentum, one moving closer to Saturn while the other moves further away. Their mass ratio is $\sim 3:1$, and modeling of the libration has yielded increasingly accurate masses for both objects (Yoder et al. 1989; Nicholson et al. 1992; Jacobson et al. 2008).

The present configuration is stable, but the outward migration of the satellites due to their gravitational interaction with the A ring¹ is likely to lead eventually to a 'tightening' of the co-orbital resonance, and its conversion from horseshoe motion to a Trojan-style libration of Epimetheus about the L_4 or L_5 point of Janus (Lissauer et al. 1985).

2.3 Ring-Embedded Moons

Between the orbits of the coorbital satellites and that of Enceladus, Cassini discovered four small moons, three of which are in MMRs with the mid-sized satellite Mimas and each of which is closely associated with either a diffuse ring or a partial ring (sometimes referred to as a 'ring arc').

The sub-km-sized satellite Aegaeon is actually embedded within the G ring (Hedman et al. 2010), a diffuse ring located midway between the orbits of Janus and Mimas and discovered by Pioneer 11. Cassini's discovery of Aegaeon resolved a long-standing mystery as to this ring's origin, which is now thought to arise from material ejected from Aegaeon as a result of impacts by interplanetary objects. Aegaeon is trapped in a 7:6 inner MMR with Mimas, as is the concentration of G ring particles that forms a distinct arc surrounding that moon.

The other three moons, Methone, Anthe and Pallene are located between the orbits of Mimas and Enceladus (Hedman et al. 2009). Anthe is in a 10:11 outer MMR with Mimas (Cooper et al. 2008), while Methone is in a 14:15 outer resonance (Spitale et al. 2006). Each is associated with a partial ring or arc that appears to be trapped in the same MMR, but lengthy libration periods of 1–2 yr make this difficult to prove observationally. Pallene, on the other hand, is associated with a narrow but azimuthally-complete dusty ring. It is very close to, but apparently not trapped in, a 19:16 inner MMR with Enceladus (Cooper et al. 2015).

These four satellites seem very likely to be the ultimate sources of the associated ring material, which is probably ejecta produced by high-velocity impacts of interplanetary dust particles, in the same manner that the jovian rings are believed to be derived from its embedded moons (Burns et al. 1999). The added wrinkle here is that, at least for Aegaeon, Methone and Anthe, some or all of this ejecta remains trapped in the same resonance as its parent moon, and thus forms an arc rather than a complete ring.

¹More precisely, the reaction torque associated with the several strong density waves driven in the main rings by the satellites; see the discussion in Sect. 5.

3 Radii, Masses and Mean Densities

The radii, masses and mean densities of the inner small moons, where known, are summarized in Table 2, adapted from Thomas and Helfenstein (2020) and references therein. The masses listed here are based on analysis of their mutual gravitational perturbations or — in the case of Pan and Daphnis — their effects on the nearby rings. Helene's mass has recently been estimated from its perturbation of the orbit of Dione (Jacobson 2022). In the case of Aegaeon, Methone and Pallene, their near-ellipsoidal shapes have been used to estimate their densities directly, assuming hydrostatic equilibrium (Thomas et al. 2013).

The most striking feature here is the low densities; all but Anthe — whose mass and density are unknown — have mean densities appreciably less than that of pure water ice ($\sim 920 \text{ kg m}^{-3}$), and at least a factor of two less than that of the saturnian mid-sized satellites. The implication is that all of these objects are extremely porous, with a fraction of void space (or porosity) ranging from at least 30% for Janus and Epimetheus to at least 70% for Methone and Pallene, even assuming a negligible rocky component. The mean densities vary systematically with the objects' sizes: from a minimum of $\sim 250 - 300 \text{ kg m}^{-3}$ for Daphnis, Pallene, and Methone, to $\sim 400 \text{ kg m}^{-3}$ for Pan and Atlas, $\sim 500 \text{ kg m}^{-3}$ for Prometheus and Pandora, and 630 kg m^{-3} for Janus and Epimetheus. In this respect, the smallest ring moon Aegaeon is an exception, with a density of $\sim 540 \text{ kg m}^{-3}$. Particularly noteworthy is the similarity in density shown by the pair of co-orbitals and by the two F ring shepherds. The trends seen in the ring-moon densities suggest an internal compression that increases with size, though even Janus and Epimetheus have very low central pressures, of order $3 \times 10^5 \text{ Pa}$.

As is elaborated on in Sect. 5, the very high porosities are more consistent with the hypothesis that these objects accreted from ring material than with the idea that they are collisional shards resulting from the destruction of larger satellites, though we discuss below the possibility that all or many of these moons may harbour a denser core, which may be such a collisional shard.

Support for the accretional model is provided by the distinctive 'flying-saucer' shapes of Pan and Atlas, as revealed in high-resolution Cassini images (Porco et al. 2005, 2007; Charnoz et al. 2007; Buratti et al. 2019), whose prominent equatorial ridges might be due to ongoing accretion of icy material from the adjacent rings. Further discussions of the sizes, shapes and surface morphologies of the inner moons are to be found in Porco et al. (2007), Thomas et al. (2013, 2018b), Buratti et al. (2019), and Rambaux et al. (2022) as summarized in Sect. 4 below.

4 Ring Moon Shapes and Morphology

Ring moons range from a few kilometers to $\sim 100 \text{ km}$ in radius (see Table 2), and many of these low-density, highly tidally constrained, rapidly rotating satellites exhibit irregular shapes. Figure 1, adapted from Thomas et al. (2018b), illustrates the diversity of shapes of these satellites in the context of Saturn's small moons. The images were acquired by the Cassini spacecraft during its journey through the saturnian system and especially at the end of the mission during the Grand Finale orbits. The shapes vary from ravioli-like structures with an equatorial ridge (Atlas, Pan and Daphnis), to elongated ones for Prometheus and Pandora, irregular covered with craters for Janus and Epimetheus, and the surprising smooth triaxial ellipsoids of Methone, Pallene and Aegaeon.

Table 2 Radii, masses, mean densities, surface gravities, albedos, and brightness coefficients for Saturn's small moons. For each satellite the best spatial resolution of ISS NAC images is reported

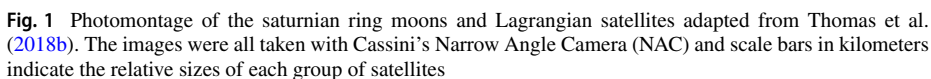
Satellite	R_{mean} (km)	Mass (kg)	ρ (kg m ⁻³)	g (mm s ⁻²)	Albedo ² ($\alpha = 10^\circ$)	Brightness Coefficient ³ ($\alpha = 30^\circ$)	ISS NAC images best sp. res. (km/pixel)
Pan	13.7 ± 0.3	4.30 ± 0.22 × 10 ¹⁵	400 ± 31	0.1-1.7	0.52 ± 0.04	0.6492 ± 0.0058 ± 0.0142	1.269
Daphnis	3.9 ± 0.5	6.8 ± 1.7 × 10 ¹³	276 ± 144	0.0-0.3	0.56 ± 0.04	-	0.438
Atlas	14.9 ± 0.2	5.753 ± 0.015 × 10 ¹⁵	412 ± 19	0.1-1.7	0.49 ± 0.08	0.6254 ± 0.0084 ± 0.0084	0.190
Prometheus	42.8 ± 0.7	1.500 ± 0.009 × 10 ¹⁷	460 ± 21	0.7-5.6	0.67 ± 0.07	0.7928 ± 0.0127 ± 0.0130	0.201
Pandora	40.0 ± 0.3	1.3684 ± 0.013 × 10 ¹⁷	509 ± 12	2.2-6.1	0.62 ± 0.08	0.7600 ± 0.0053 ± 0.0057	0.312
Epimetheus	58.6 ± 0.3	5.2605 ± 0.0013 × 10 ¹⁷	625 ± 8	6.6-10.9	0.41 ± 0.04	0.5305 ± 0.0082 ± 0.0027	0.154
Janus	89.0 ± 0.5	18.9548 ± 0.0045 × 10 ¹⁷	642 ± 10	11.1-16.9	0.37 ± 0.03	0.4628 ± 0.0060 ± 0.0026	0.178
Aegaeon ¹	0.33 ± 0.06	7.82 ± 3.00 × 10 ¹⁰	539 ± 140	0.009-0.013	0.25 ± 0.23	0.1793 ± 0.0050 ± 0.0326	0.091
Methone ¹	1.45 ± 0.03	3.92 ± 1.00 × 10 ¹²	307 ± 30	0.081-0.013	0.42 ± 0.05	0.5558 ± 0.0033 ± 0.0115	0.027
Anthe ⁴	< 1?						5.290
Pallene ¹	2.23 ± 0.07	1.15 ± 0.40 × 10 ¹³	251 ± 75	0.011-0.016	0.29 ± 0.11	0.5228 ± 0.0066 ± 0.0164	0.220
Telesto	12.3 ± 0.3				0.61 ± 0.04	0.9028 ± 0.0100 ± 0.0220	0.063
Calypso	9.5 ± 0.4				0.69 ± 0.14	1.0999 ± 0.0176 ± 0.0463	0.136
Helene	18.1 ± 0.2	7.1 × 10 ¹⁵	291 ± 8		0.74 ± 0.15	1.0251 ± 0.0148 ± 0.0113	0.411
Polydeuces	1.3 ± 0.3				0.86 ± 0.06	0.6075 ± 0.0089 ± 0.0794	0.012

¹Density & gravity inferred from shape

²Cassini ISS CL1/CL2, 610 nm

³The first error bars are statistical, and the second are systematic errors due to uncertainties in the moon's average size

⁴From Thomas et al. (2018b)



Most notably, Thomas and Helfenstein (2020) discuss Digital Terrain Models (DTMs; shape data are from Thomas et al. 2018a, available in the Planetary Data System) that provide descriptions of the shapes of the bodies in terms of tessellated plate models whose estimated radial uncertainties range from tens to hundreds of meters. Recently, spherical

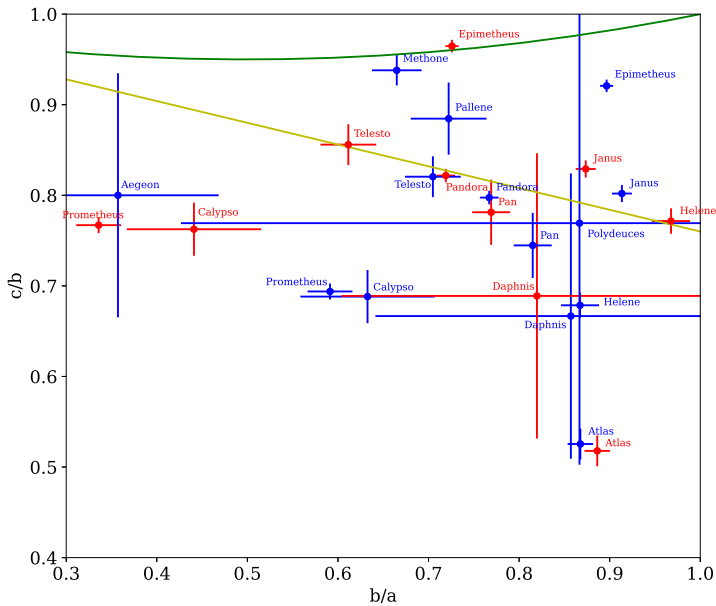


Fig. 2 Principal axis ratios b/a and c/b with their uncertainties for the small satellites of Saturn. The green curve represents the expected trend for a Roche ellipsoid configuration. The yellow curve is the “Omega sequence” of Dobrovolskis (2019). Blue points are from the best-fit ellipsoids of Thomas and Helfenstein (2020) and red points are from the degree-2 ellipsoid shapes of Rambaux et al. (2022) after spherical harmonic decomposition (figure adapted from Rambaux et al. 2022)

harmonic analysis of these DTMs has continued this descriptive work, to describe some geological features and to estimate fundamental quantities such as gravitational coefficients and librational amplitudes (Rambaux et al. 2022).

The hydrostatic equilibrium shape of a body in a strong tidal environment is specified by the Roche ellipsoid (Roche 1851; Chandrasekhar 1969). The first Cassini observations of ring moons and their analysis suggested that these bodies had accreted around an initial seed with shapes close to the appropriate Roche ellipsoid (computed using Roche lobe procedure in Porco et al. 2007). However, subsequent observations have led to more precise values of the semi-major axes of the best-fit ellipsoids (Thomas and Helfenstein 2020), whose ratios (c/b vs b/a) are reported in Fig. 2, indicating a departure from the values expected in Porco et al. (2007). In addition, the topography is disturbed by geological structures at various morphological wavelengths, such as ridges and depressions, or by impact processes that modify the final shapes for highly cratered bodies.

Rambaux et al. (2022) proposed to use the spherical harmonic decomposition to filter out the effect of craters (corresponding to short surface wavelengths) and to extract the global shape from the degree-2 coefficients (long wavelengths). The spherical harmonic decomposition is fitted to the DTM and computed until degree-14 for most satellites to obtain accurate low-degree harmonics, representing the shape underneath the cratered surface. The values of the semi-major axes ratio determined by this method are shown in Fig. 2. Among the ring moons only Epimetheus comes closer to the Roche ellipsoid curve. The ring satellites Pandora, Pan, Janus and the small bodies Telesio and Helene are closer to the so-called “Omega sequence” line defined by Dobrovolskis (2019). This curve represents the special case when the rotational velocity above which the force is repulsive at the ends of the a -axis (Ω_0) is

equal to the rotation velocity for which the gravity potential along the meridian $x = 0$ (passing through the b and c axes) is constant and maximum (Ω_{bc}). Thus, if the satellite rotates at this rotation velocity $\Omega_0 = \Omega_{bc}$, any cohesionless material on the surface would accumulate at the ends of the a -axis (being potential minima) and the repulsive force will eject the material. In this configuration cohesionless regolith should be removed from the surface, however such scenarios would require a fast rotating body (at $\Omega_0 = \Omega_{bc}$) with rotation period of about 1 to 2 hours that is 20 to 60 times faster than the present rotational rate.

Some bodies appear to be more flattened (ratio $c/b < 0.8$) and/or more elongated (ratio $b/a < 0.8$) than the Roche ellipsoid configuration or the Omega sequence. Such variety of shapes provide some clues on the formation scenarios of these objects and is the result of possibly different histories (see also Sect. 5). Atlas, Daphnis, and Pan present equatorial ridges, which may have resulted from either the deposition of ring material on an initial object (Charnoz et al. 2007; Quillen et al. 2021) or from low-velocity collisions (Leleu et al. 2018), while the shape of elongated bodies such as Prometheus and Calypso might be more consistent with the latter mechanism.

Many of these satellites have distinctive geologic structures illustrating unique histories not yet included in any global scenario of satellite formation. Here we detail six of these features, based on studies by Porco et al. (2007), Thomas (2010), Thomas et al. (2013), Thomas and Helfenstein (2020) and Rambaux et al. (2022).

- (i) The aforementioned equatorial ridges of Atlas, Pan and Daphnis. Such features are few kilometers above a presumed crestless body for Atlas and Pan, and tens of meters for Daphnis. The latitudinal spread of these bands is around $\pm 20^\circ$ for Atlas, $\pm 15^\circ$ for Pan, while Daphnis is characterized by two small off-center equatorial ridges centered at 2° S and 22° N (see Fig. 10 of Thomas and Helfenstein (2020) and Fig. 3 of Buratti et al. (2019)). It has been noted that these equatorial ridges have a polygonal longitudinal structure, as illustrated in the silhouettes shown in Fig. 5 of Thomas and Helfenstein (2020) or in the spherical harmonic mappings in the Appendix of Rambaux et al. (2022) (Figs. A.1 and A.7).
- (ii) Spherical harmonic decomposition shows that the satellites Calypso, Pandora, and Prometheus have pronounced north-south longitudinal bands visible at degree-4 similar to those of Bennu and Ryugu (Roberts et al. 2021) despite their very different sizes.
- (iii) It is noticeable that these three bodies are also quite elongated toward Saturn. The two satellites Daphnis and Telesto also show signs of elongation.
- (iv) Helene and Telesto show large degree-3 spherical harmonics leading to a high-latitude offset of the topography of $+40^\circ$ and $+15^\circ$ respectively.
- (v) Janus and Epimetheus do not show a clear pattern for the high-degree coefficients of their topography. This behavior could be the result of important processes of surface craterization as directly visible in the images of these two satellites.
- (vi) Finally, several of these satellites show grooves, or long linear depressions in the regolith covering their surfaces (Morrison et al. 2009; Thomas and Helfenstein 2020). The origin of these grooves is not yet well understood and several scenarios have been proposed such as fracturing of the body below the regolith, secondary impacts, or even fissures in regolith (e.g. Asphaug 2020). Tidal stresses as for the grooves on Phobos seems unlikely because the satellites are beyond the synchronous orbit and are thus moving away from Saturn (Thomas et al. 2018b).

5 Ring Moon Origins and Evolution

The origin of moons within the ring system is not an easy thing to explain. Indeed forming icy satellites within the Roche Limit of Saturn for ice, is, by definition, prevented by the tidal forces from the planet. Accretion of ring material into moonlets is only possible beyond some distance where the self-gravity of the moonlet exceeds the planet's tidal force. But there are many definitions of the Roche Limit, depending on the details of the physics that is considered (pure gravity, frictional forces, etc.). The general form of the Roche Limit is given by:

$$R_L = k R_P \left(\frac{\rho_P}{\rho_r} \right)^{1/3} \quad (1)$$

where R_P and ρ_P are the planet's radius and average density, ρ_r is the density of the ring material and k is a prefactor that depends on the physics that is considered. For the case of non-porous ice $\rho_r \simeq 900 \text{ kg m}^{-3}$, but studies of self-gravity wakes in Saturn's rings suggest that the ice may be very porous, with an average density of $\sim 420 \text{ kg m}^{-3}$ (Porco et al. 2008). For a cohesionless body $k = 2.4552$ (Chandrasekhar 1969).

Holsapple and Michel (2006) argue that we should consider two different versions of the Roche Limit. The "Fluid Roche Limit" (FRL) for a cohesionless body is the minimum distance at which material can accrete from the ring material into a self-gravitating object. For Saturn's rings the Fluid Roche Limit is $\sim 2.43 R_P \simeq 132,000 \text{ km}$ for icy material with a density of 900 kg m^{-3} , but is much further from the planet for lower density material. Porco et al. (2007) reports that densities of Saturn's inner moons are all lower than 900 kg m^{-3} suggesting that they are all currently orbiting inward of their Fluid Roche Limit. Dermott et al. (1979) have shown that a satellite evolving inward its Fluid Roche Limit may lose material from its surface and feed the surrounding system, leading to a complex interplay between the satellite and the rings, implying also modifications of its shape. If it evolves inward, at some point it should break into objects small enough for their tensile stress to counter-balance tides. This is the "Rigid Roche Limit" (RRL, see Holsapple and Michel 2006, for a detailed calculation), that is the distance at which an already-constituted satellite with tensile stress is destroyed by tides. Whereas a body with no material resistance may be formed or destroyed at the FRL, the RRL may be well inside the FRL for the same density because (i) the body may have a non-hydrostatic shape, and (ii) internal cohesion within the satellite (as measured by the friction angle for example) acts against its destruction. So an already constituted object may survive against tides, inward the region where it formed, because of internal material resistance. For example a body with the same density ($\sim 640 \text{ kg m}^{-3}$) and shape as Janus has a fluid Roche Limit at $\sim 151,000 \text{ km}$ from Saturn, but would have a rigid Roche Limit of $\sim 108,000 \text{ km}$ for an assumed friction angle of 20° (Holsapple and Michel 2006).

The take-home message is that if ring-moons are only made of water ice with the same average density as the surrounding ring particles themselves, it does not seem easy that they could form spontaneously at less than $\sim 130,000 \text{ km}$ from Saturn for non-porous ice, and $\sim 168,000 \text{ km}$ for porous ice. However, once formed they might survive against tidal disruption down to about $\sim 110,000 \text{ km}$.

Gravitational accretion of a swarm of particles in a disk under the tidal forces of the planet ("tidally modified accretion") was theorized by Canup and Esposito (1995, 1996). They study the conditions under which colliding particles may gravitationally stick under the effect of inelastic collisions. They found two necessary conditions: the final size of the

body must be less than the Hill sphere of the equivalent mass body, and the final energy must be negative in the local rotating frame (Eqs. 28 to 30 in Canup and Esposito 1995). As a result the closer the bodies to the planet, the more dissipative the collision must be in order for them to stick. For equal size bodies, if the sum of their radii is larger than about 70% of their mutual Hill radius, then capture is impossible because the two-bodies would overflow their mutual Hill sphere. As the Hill Sphere radius is proportional to the distance to the planet ($R_H = a_s(m/(3M_P))^{1/3}$ where R_H , a_s , m and M_P are the Hill radius, the distance to the planet, the body mass and the planet's mass respectively), this condition becomes more and more restrictive closer to the planet. For particles accreting in Saturn's A ring, the mass-ratio of two colliding particles must be less than 0.01 to stay gravitationally bound (Table 1 of Canup and Esposito 1995). As a result, local simulations of accretion in such a tidally modified environment show that growth is strongly limited: larger bodies can only grow by accumulating much smaller objects, while small particles are gravitationally scattered. This results in bi-modal size distribution where "moonlets" co-exist with a swarm of high-velocity and small particles. However the largest objects have about the same size as the largest initial particles in the system, since they just accumulate a layer of small particles. The resulting size of the largest objects is then similar to that of the largest objects that were put at the start of the simulation. In these conditions it seems very difficult to grow spontaneously objects as big as Pan or Daphnis from a swarm of cm or meter sized particles. This may suggest that moonlets in the A ring may be formed by some other process, or that a big initial seed (or shard) must have been present. Canup and Esposito (1995) assumed that all particles have the same density, but allowing particles to have different densities (like porous and dense ice, or silicate-rich material) may offer interesting possibilities.

For these reasons, it has been proposed (Porco et al. 2007; Charnoz et al. 2007) that the inner ring moons may have formed from material with a density higher than that of typical ring particles, such as silicate-rich material or dense ice with low porosity (originating, maybe, from the formation of the rings via tidal destruction of a satellite or a passing object; Crida et al. 2024, this collection). The favored scenario would be a shard of dense material covered with much lower-density ring particles. If a silicate chunk is embedded within the rings it will accumulate ice-rich small particles up to a limit where the ringmoon's Hill sphere is completely filled with material, beyond which material cannot be accreted anymore. As shown in (Porco et al. 2007) there exists a critical moon density, ρ_c below which accretion is not possible anymore, $\rho_c = M_P/(\eta a_s^3)$ where M_P is the planet's mass, a_s the satellite's semi-major axis, and $\eta \sim 0.53$ (this factor arises from the volume of the Hill sphere; Charnoz et al. 2011). As long as the ringmoon density is $> \rho_c$ accretion continues indefinitely, but it stops when the moon's mean density is equal to ρ_c . At the distance of Pan, $\rho_c \sim 450 \text{ kg m}^{-3}$, very close to Pan's estimated density of about 420 kg m^{-3} (Porco et al. 2007). This is why Charnoz et al. (2007) and (Porco et al. 2007) propose that a dense shard may be embedded in all ringmoons.

In summary, the processes described above suggest that two "formation" mechanisms may still be active in Saturn's rings. (i) Any chunks of dense material (or any material denser than the Roche Critical density, ρ_c) may rapidly capture an icy envelope made of ring material, and then be viscously transported outward. This scenario may be relevant for all ring-moons that are — or once were — embedded in the A ring. (ii) The concurrent process is the spontaneous accretion of icy ring material at or near the Fluid Roche Limit of Saturn (beyond the A ring, typically) that may form new ring-moons via gravitational instability. This second process may take place in Saturn's F ring also, giving birth to a population of transient moonlets detected inside this ring (Beurle et al. 2010).

In this context, two alternative processes have been proposed to explain the ring moons' observed shape described in Sect. 4. In the first case, it is the result of the accretional process

of ring material onto this initial seed (Charnoz et al. 2007; Quillen et al. 2021). In this scenario, as the body migrates outwards, material from the rings falls onto its equator and forms the equatorial ridge seen around some moons. In the second case, the shape of the moon is produced during a low-impact-angle and slow-speed collision between two similar progenitors (Leleu et al. 2018). Such a process is in agreement with the pyramidal regime where bodies of similar sizes accrete to form larger bodies (Charnoz et al. 2010; Crida and Charnoz 2012), and could not only reproduce the ravioli-like shapes but also the highly elongated shape of Prometheus.

After their formation, the larger objects would have evolved rapidly outwards due to gravitational torques exerted by the nearby ring material.² Embedded ring-moons, if they are large enough to open a gap in the rings (like Pan or Daphnis), will evolve according to the so-called “Type 2” migration scenario (see, e.g. Crida et al. 2010) and remain “locked” in the rings, simply following the ring’s viscous evolution. This process may be relevant for moonlets embedded in the A ring, but not for isolated moonlets beyond Atlas. Simulations of the rings’ viscous evolution show that beyond $\sim 120,000$ km the rings should spread outward (neglecting the torques exerted by moons exterior to the rings) (Salmon et al. 2010).

The smallest of the present ring moons, Daphnis and Pan, are securely imprisoned within their respective gaps, but presumably will emerge from the rings in due course as the A ring edge moves outwards across the Roche limit for icy bodies and the ring material is converted into more moonlets (Charnoz et al. 2010; Tajeddine et al. 2017a). These moons may have accreted relatively recently in the overall history of Saturn’s rings. If the ring moons do not open a full gap, then their dynamical evolution may be much more complex, and maybe even stochastic as in the case of “propellers” (see e.g. Tiscareno et al. 2008; Crida et al. 2010; Spahn et al. 2018)).

Once outside the rings, the radial evolution of the ring moons will accelerate due to what is now a one-sided torque from the rings. Since this torque scales as the square of the satellite’s mass, in a manner analogous to tidal torques between planets and satellites, larger moons will drift outwards more rapidly than their smaller cousins, leading inevitably to collisions and subsequent mergers into a smaller number of progressively larger objects. This process naturally leads to a sorting of the resulting objects, with younger, smaller moons close to the rings and older, larger ones further away, similar to what is observed at Saturn. Indeed simulations of ring viscous evolution evolution coupled to moonlets formation at the Fluid Roche Limit show that masses and locations of moons inward of Mimas are reproduced, at least qualitatively (Charnoz et al. 2010). The end product is a few larger satellites such as Janus and Epimetheus.

The time for a moon to move from the edge of the A ring to the distance of the F ring depends on its mass, but is typically a few 10^5 s to ~ 100 Myr.

Although the outer edge of the A ring is currently defined by the 7:6 MMR with Janus (Spitale and Porco 2009; El Moutamid et al. 2016; Nicholson et al. 2018), this presumably was not always the case and will not be in the distant future, when Janus will have moved further away from the rings and this particular resonance will no longer coincide with the FRL for ice.

Tajeddine et al. (2017a) have estimated the tidal and ring torques on the current satellites and their resulting radial drift rates \dot{a} , as summarized in Table 3. The ring torque on each satellite was obtained by summing over the contributions from all of the particular satellite’s Lindblad resonances that fall within the main rings, combined with the ring surface mass

²Note that for all moons interior to Mimas, the ring torques significantly exceed the torque due to tides raised in Saturn, at least for $Q_{\text{Saturn}} > 10^3$; see Table 3 below.

Table 3 Radial evolution timescales for Saturn's inner moons due to saturnian tides¹ and ring torques. (Adapted from Tajeddine et al. (2017a))

Satellite	Δa (km)	\dot{a}_{Saturn} (km/Myr)	\dot{a}_{rings} (km/Myr)	τ_{orb} (yr)	Notes
Pan	−3190	0.036	90.1	3.5×10^7	2
Atlas	900	0.047	233	3.9×10^6	3
Prometheus	2610	1.06	274	9.5×10^6	4
Pandora	4940	0.83	44.2	1.10×10^8	4
Janus	14,680	8.0	39.5	3.1×10^8	5
Epimetheus	14,680	2.2	10.8	1.13×10^9	5
coorbital res.	−32	—	−4.4	7.3×10^6	6
Mimas	48,770	46.4	4.7	9.5×10^8	7

¹ Assuming that $k_2/Q_{\text{Saturn}} = 1.59 \times 10^{-4}$, or $Q_{\text{Saturn}} = 1600$. (Lainey et al. 2012)

² Neglecting shepherding torques from the Encke Gap edges

³ Neglecting retarding effects of Prometheus 54:53 resonance

⁴ Neglecting Prometheus/Pandora/F ring interactions and transient Epimetheus resonances

⁵ Neglecting capture into coorbital resonance

⁶ From Lissauer et al. (1985), updated to current masses and ring surface density

⁷ Neglecting retarding effects of Tethys 4:2 resonance

densities determined by Tiscareno et al. (2007). They found orbital evolution timescales $\tau_{\text{orb}} = \Delta a / \dot{a}$, where Δa is the present distance of the moon from the edge of the A ring, that range from 4×10^6 yr for Atlas to 3×10^8 yr for Janus and ~ 1 Gyr for Epimetheus and Mimas. The shorter time scales for the inner satellites, despite their smaller masses, reflect the fact that Δa is much smaller, as well as the larger number of first-order resonances that fall within the A and B rings.

However, Tajeddine et al. (2017a) note that these evolutionary time scales are uncertain because (i) the drift rates would have been faster when the satellites were closer to the A ring, while (ii) the satellites would have been smaller in the past if the present bodies are the result of mergers, leading to slower drift rates. These calculations update earlier estimates by Borderies et al. (1984), who assumed higher ring surface mass densities and (probably) satellite masses corresponding to solid ice, leading generally to faster evolution rates.

Goldreich and Tremaine (1982) first recognized that the orbital expansion of the small-moons outward and interacting with the A ring is much shorter than the age of the Solar System (from 20 Myrs to 200 Myrs). They proposed that some resonance with other Saturn satellites may stabilize their expansion (without identifying them) or that gap-opening within the A ring may have lowered the ring-torque they experience, and thus increase the timescale of their orbital expansion.

The orbital history of the ring moons is indeed complicated by the likelihood of capture into, and possibly escape from, mean motion resonances between various pairs of satellites during their radial migration (Poulet and Sicardy 2001; Cooper et al. 2015).

Numerical integration of the current orbits of the inner satellites by Cooper et al. (2015) have identified several examples. In addition to the 54:53 MMR between Atlas and Prometheus, mentioned in Sect. 2 above, these authors found transient 17:15 MMRs between Prometheus and Epimetheus and 21:19 MMRs between Pandora and Epimetheus,

both of which are dependent on the latter's coorbital phase. Earlier numerical integrations also showed temporary resonance trapping and orbital 'chaos' in the ring-moon system (Poulet and Sicardy 2001). The existence of such resonances, even temporary ones, means that the timescales in Table 3 are likely to be lower limits, inasmuch as the resonance will effectively act to transfer a portion of the ring torque on the small, inner moon to the more massive, outer moon, in such a way as to maintain a constant ratio of orbital periods.

An interesting special case is the coorbital resonance between Janus and Epimetheus, the largest ring moons interior to Mimas. Lissauer et al. (1985) studied the effect of ring torques on this resonance, finding that it is rapidly tightening over time (*i.e.*, the current 48 km separation between the two satellites' orbits is decreasing). Updating their numerical values, we find that the age of this resonance is only ~ 7 Myr, and that it will be converted into a Trojan-style configuration in another 9 Myr.

Also, Lissauer et al. (1984) noted that, for the current orbit of Janus, its strong 2:1 density wave falls only a few hundred km outwards of the unique 'flat spot' in the inner B ring, at which location Janus would probably have been trapped in the 2:1 MMR with Enceladus. They suggested that a disruptive collision some 10^8 or so years ago may have freed Janus from this resonance.

Although none of the existing ring moons is in resonance with any of the mid-sized satellites at the present time, Borderies et al. (1984) pointed out that Pandora is only ~ 180 km interior to the 3:2 MMR with Mimas, and that it might be expected to be captured into this resonance in the fairly near future. Such a capture would almost 'freeze' the radial evolution of Pandora, as the resonance will act to transfer the ring torque to the more massive satellite. But Tajeddine et al. (2017a) find that the outward drift rates of Pandora and the Mimas 3:2 resonance are almost equal, raising doubts as to whether or not the capture will ever occur. Mimas, in turn, is in a stable 4:2 MMR with Tethys, which is likely to slow down its orbital expansion relative to that given in Table 3. For the above reasons, the times given here should be taken as indicative of the current orbital expansion rates, but not as realistic estimates of the ages of individual moons.

In conclusion, there are many still open questions concerning the origin and evolution of the small moons of Saturn. Do they form a long-lived or a transient population? When did they form? Are they as old as the main ring system or much younger? See also Crida et al. (2024, this collection) for more discussion.

6 Composition and Regolith Physical Properties

As of writing, the investigation of the physical and compositional properties of the regolith covering the surface of the ring moons was made possible through the extensive observation campaigns carried out by remote sensing instruments onboard the Cassini mission, namely the Imaging Science Subsystem (ISS; Porco et al. 2004), the Visible and Infrared Mapping Spectrometer (VIMS; Brown et al. 2004), and the Ultraviolet Imaging Spectrograph (UVIS; Esposito et al. 2004). These experiments characterized the spectrophotometric properties of the ring moons over a broad wavelength interval, from the far-UV to near-IR ($\sim 0.1 - 5.1 \mu\text{m}$).

In this section we provide a summary of the main results from remote sensing observations of the ring moons, reporting on 1) their photometric properties at visible wavelengths (Sect. 6.1), 2) UV-VIS-IR spectroscopic investigations (Sect. 6.2), and 3) results of spectral modeling efforts (Sect. 6.3). The ring moon data are discussed in the broader context of the spectrophotometric properties of Saturn's mid-sized icy moons and main rings.

6.1 Visual Albedos and Photometric Properties

Thus far, there have not been many detailed photometric studies of Saturn's smaller moons simply because the available data are rather limited. For example, Cassini was unable to observe most of these moons at phase angles below 1° , so there is little information about the magnitude and extent of their opposition surges (Thomas et al. 2018b). Thus the only small moons with reasonably secure geometric albedos are Janus and Epimetheus, which are large enough to be observed with Earth-based telescopes such as HST. Interestingly, Verbiscer et al. (2007) found that these objects have geometric albedos of 0.71 ± 0.02 and 0.73 ± 0.03 , respectively, significantly lower than those of the mid-sized satellites Mimas, Enceladus, Tethys, Dione and Rhea. They attributed this to the fact that the coorbital moons are in a region that probably has a much lower flux of the E-ring particles that are thought to coat the surfaces of the mid-sized satellites.

More recently, Thomas et al. (2018b) estimated whole-disk albedos for Saturn's satellites, including the small moons, at an effective phase angle (α) of 10° using extrapolations of the available Cassini photometric data (see Table 2). These numbers are somewhat lower than the geometric albedos (which are evaluated at 0° phase by definition), but generally follow similar trends with orbital location, confirming the importance of E-ring flux to the moons' brightnesses. Generally, among the ring moons, the albedos are highest for Prometheus and Pandora, perhaps due to a coating of icy material from the nearby F ring, somewhat lower for the inner ring moons and the coorbitals, and lowest for the ring-embedded moons, Aegaeon, Methone and Pallene. These three objects are darker than expected, suggesting that other processes might be influencing the smallest moons' surface brightness.

One limitation with the albedo estimates for the small moons derived by Thomas et al. (2018b) is that they have rather large error bars. These uncertainties are not primarily due to errors in the measured brightness of the moons, but instead arise because these moons are far from spherical and so the apparent brightness of the moon depends not only on its phase angle but also on the orientation of the moon relative to the observer and the Sun, which is not accounted for in standard albedo calculations.

To address these issues and provide tighter constraints on the moons' light-scattering properties, Hedman et al. (2020) used a technique that accounts for the varying lighting geometry across each moon's surface. Specifically, they estimated a phase-dependent ratio of the moon's observed brightness at a wavelength of 650 nm to its predicted brightness, assuming that its shape is a perfect ellipsoid and that its surface follows a perfect Lambertian or Minnaert scattering law. This ratio is referred to as the "brightness coefficient", and below we provide a brief description of how it is derived. The observed brightness can be expressed in terms of the effective area of the target A_{eff} ,³ given by

$$A_{eff} = \sum_x \sum_y I/F_{x,y} \Omega_{pixel} D^2 \quad (2)$$

where $I/F_{x,y}$ is the measured radiance factor of the pixel x, y in the target image, Ω_{pixel} is the solid angle subtended by the pixel, and D is the distance from the target. Assuming that the surface reflectance R follows a Minnaert scattering law, this is given by $R = B(\cos i)^k (\cos e)^{1-k}$ (notice that $k = 1$ reduces to the Lambertian case), where B is

³This is the equivalent area of a target with $I/F = 1$ required to provide the observed brightness

the “brightness coefficient” (a phase-dependent factor, constant for each image). Thus, the predicted brightness can be expressed in terms of the predicted effective area given by

$$A_{pred} = \int_{++} B(\cos i)^k (\cos e)^{1-k} (\cos e) r_{eff}^2 \cos \lambda d\lambda d\phi, \quad (3)$$

where the integral is performed over the portion of the target both illuminated and observed ($++$), λ and ϕ are latitude and longitude on the object, and r_{eff} effective radius. For an ellipsoidal object with dimensions a , b , and c , the effective radius is given by

$$r_{eff}^2 = [b^2 c^2 \cos^2 \lambda \cos^2 \phi + a^2 c^2 \cos^2 \lambda \sin^2 \phi + a^2 b^2 \sin^2 \phi]^{1/2} \quad (4)$$

Then, B can be straightforwardly derived by equating A_{eff} and A_{pred} , providing:

$$B = \frac{A_{eff}}{\int_{++} (\cos i)^k (\cos e)^{1-k} (\cos e) r_{eff}^2 \cos \lambda d\lambda d\phi}, \quad (5)$$

where A_{eff} is obtained from observations and the denominator can be computed numerically. As anticipated above, the “brightness coefficient” is a function of the phase angle (through A_{eff}), and as such it does not equal the moon’s classical geometric or Bond albedo. Nonetheless, trends in the brightness coefficients across Saturn’s larger moons match the trends in their geometric albedos, making it a useful parameter for comparing how efficiently the surfaces of different moons scatter light. Furthermore, the scatter in this quantity among images taken at similar phase angles is much smaller than that of the classical geometric albedo.

Figure 3 shows the brightness coefficients at a phase angle of 30° for all of Saturn’s moons interior to Titan (see also Table 2 for small moons’ values). The larger moons (Mimas, Enceladus, Tethys, Dione, Rhea) show the trend of brightening with increasing E-ring flux previously observed by Verbiscer et al. (2007) and Pang et al. (1984). Furthermore, Janus, Epimetheus, Mimas, Tethys, Dione and Rhea all show longitudinal brightness variations consistent with the expected asymmetries in the E ring flux. Note that the E-ring extends across the orbits of all these moons, primarily because the E-ring particles have a wide range of eccentricities while most have semi-major axes not far from that of Enceladus’ orbit. This means that most of the E-ring particles encountering Janus, Epimetheus and Mimas are near their orbital pericenters, so they are moving faster than the moons and primarily strike their trailing sides. By contrast, the E-ring particles striking Tethys, Dione and Rhea are primarily near their orbital apocenters and so are moving slower than the moons, leading to a particle flux that is greater on the moon’s leading sides. It turns out that Janus, Epimetheus and Mimas all have brighter trailing sides, while Tethys, Dione and Rhea are all brighter on their leading sides, consistent with the basic idea that impacting E ring particles brighten the surfaces of Saturn’s moons.

However, the smaller moons show several interesting deviations from the trends observed in the larger moons, indicating that other processes are also influencing the surfaces of these moons. First of all, the smallest moons Aegaeon, Methone and Pallene are all much darker than one would predict based on the observed trend from Janus/Epimetheus to Mimas and Enceladus. All three of these moons reside within the inner flank of the E ring, which clearly influences the brightness of the larger moons. Currently, the most likely explanation for the low surface brightness of these tiny moons is that they are all exposed to much larger fluxes of high-energy charged particles, which are observed to be concentrated in regions between the rings and the orbits of the larger moons (Hedman et al. 2020).

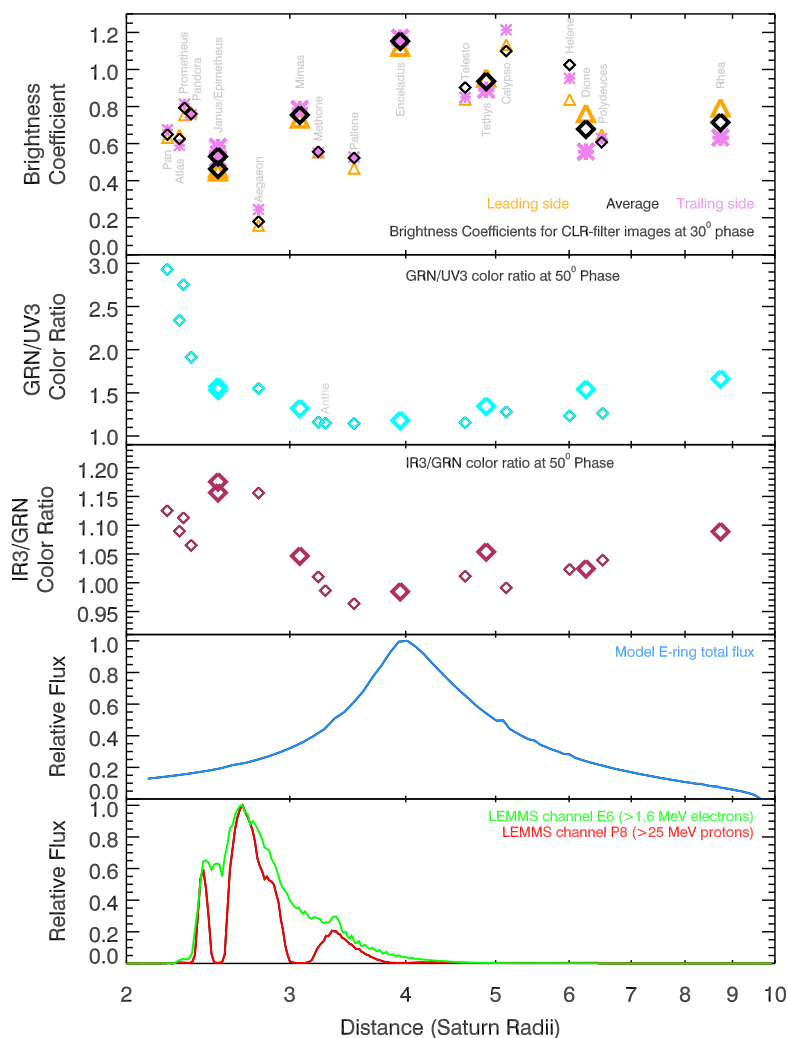


Fig. 3 Radial profiles of the brightness coefficients and GRN/UV3 and IR3/GRN color ratios of Saturn's icy moons, compared to the modeled flux of E-ring particles into the moons and the measured relative flux of high energy protons and electrons from the Cassini's Low-Energy Magnetospheric Measurement System (LEMMS) instrument (Krimigis et al. 2004). Diamonds, triangles, and asterisks refer to average, leading side, and trailing side values, respectively. The largest moons (Epimetheus, Janus, Mimas, Enceladus, Tethys, Dione, and Rhea) are indicated with larger symbols. Daphnis is not included in this plot because its signal was difficult to isolate from nearby ring material in the available low-phase images. Anthe is not included in the top panel because there were no suitable images of this moon at phase angles around 30°. Figure adapted from Hedman et al. (2020)

By contrast, several other small moons appear to be brighter than one would expect. Most dramatically, Calypso is much brighter than either Tethys or Telesto, while Helene is brighter than Dione or Polydeuces. Again, this suggests that something besides the local flux of E-ring particles is influencing the brightness of these particular bodies, although we note that Thomas et al. (2018b) report slight different albedo trend for these last objects. It

is also worth noting that Prometheus and Pandora are brighter than any of the other inner moons (Pan, Atlas, Janus and Epimetheus). Since Prometheus and Pandora both orbit close to Saturn's F ring, this suggests that material from the water-ice rich F ring may be able to brighten both of these moons (Hedman et al. 2020).

Although the discussion above is based on the investigation of the brightness coefficient of the ring moons computed at a phase angle of 30° , future studies might benefit from replicating the exercise of Hedman et al. (2020) at a phase angle of $\sim 55^\circ$. The full-disk brightness from a spherical object can be expressed as

$$I = J \frac{A_s P(\alpha)}{4}, \quad (6)$$

where J is the solar irradiance at the target heliocentric distance, α is the phase angle and $P(\alpha)$ is full-disk phase function. It can be easily shown that, for a spherical object

$$\frac{A_s P(\alpha)}{4} = \frac{B(\alpha) P_L(\alpha)}{4} \quad (7)$$

where $P_L(\alpha)$ is the full-disk phase function of a sphere whose surface follows a lambertian scattering law. Also, it is found empirically that typical full-disk phase functions of spherical objects intersect at $\sim 55^\circ$ (Cuzzi et al. 2017), thus $P(55^\circ) \sim P_L(55^\circ)$. This implies, from Eq. (7), that the brightness coefficient at 55° provides a good estimate of the target Bond albedo $B(55^\circ) \sim A_s$, allowing us to compare systematically the intrinsic albedo properties of the different targets, independently from their particular scattering behavior.⁴ We note that the above discussion is strictly valid for spherical objects, yet the described approach appears desirable also for the more or less irregular ring moons.

6.2 Colors and UV-VIS-IR Spectral Properties

Given the small size of the ring moons, and the resulting low signal levels, the VIMS experiment was only able to collect VIS-IR spectroscopic data for the brighter ones, namely Pan, Daphnis, Atlas, Prometheus, Pandora, Janus, Epimetheus, and Methone (Buratti et al. 2010; Filacchione et al. 2010, 2012, 2013; Buratti et al. 2019). The average spectra of these moons are shown in Fig. 4 and show definite similarities with the spectra of Saturn's main rings and the inner mid-sized moons. They are characterized by prominent water ice absorption features at 1.5, 2.0, and $\sim 3 \mu\text{m}$ and a significant reflectance downturn shortward of $\sim 0.55 \mu\text{m}$.⁵ The latter has been interpreted as resulting from contamination by UV-absorbing chromophores generally thought to be organic in nature (Ciarniello et al. 2011; Filacchione et al. 2013; Cuzzi et al. 2018b; Ciarniello et al. 2019, and Sect. 6.3), but for the C ring and several outer satellites an iron-rich composition has been suggested instead (Clark et al. 2012).

⁴There is some precedent for this approach. Normalized phase functions of plausible shapes tend to pass through a node in the vicinity of 50° phase angle (the so-called 'Russell's Law' of vintage planetary science lore). Thus the observed *brightness* of the object at this phase angle, which is the product of the (constant) spherical albedo and the normalized phase function, is nearly phase-function-independent. In this sense the relative values of the brightness coefficients are good proxies for the relative albedos of the objects. For more information see Veverka (1971). The shape of the phase function itself probably contains information as to the effects of shadowing due to surface roughness (Hapke 2012; Cuzzi et al. 2017).

⁵For Daphnis (where the VIS part of the spectrum is missing) and Methone (spectrum very noisy at visible wavelengths), the UV downturn cannot be characterized with VIMS data. Nonetheless, ISS multi-spectral observations of Methone indicate significant UV absorption for this target (Hedman et al. 2020).

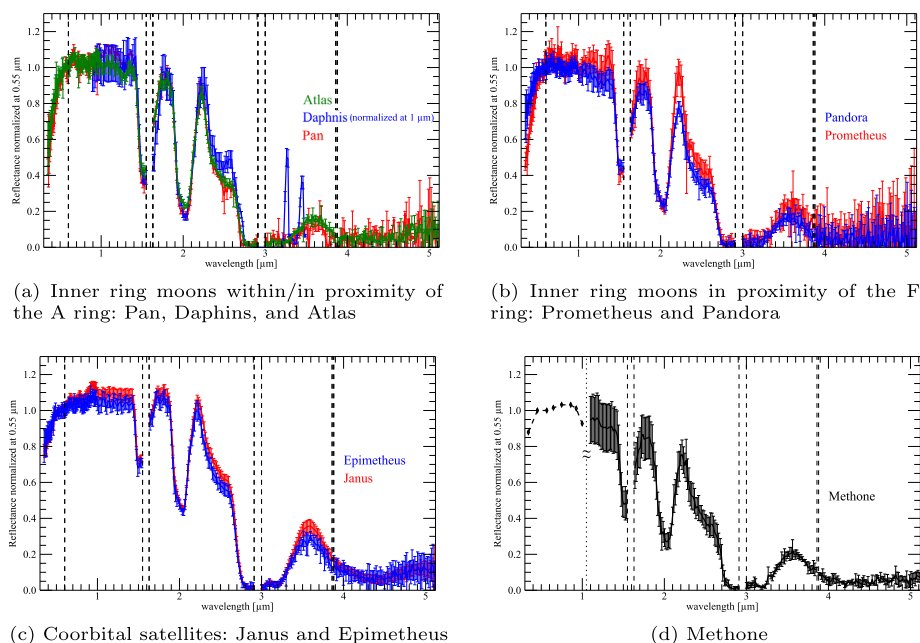


Fig. 4 Average full-disk reflectance spectra of the ring moons, as computed from available VIMS data (dashed lines indicate instrument order sorting filters junctions). See Filacchione et al. (2010, 2012) for data processing details. Before averaging, each full-disk spectrum from a given observation of the selected target has been corrected to a reference phase angle of 50° (see Appendix A), in order to minimize spectral variability induced by varying observation geometry (Ciarniello et al. 2011; Filacchione et al. 2022). Methone reflectance at visible wavelengths is from ISS observations in different filters interpolated at 57.7° phase angle, and further corrected to 50° phase angle. The corresponding IR part of the spectrum, from VIMS observations, has been arbitrarily scaled around a putative water ice absorption at $1.05 \mu\text{m}$ (dotted line), so that the reflectance at $1.098 \mu\text{m}$ (right shoulder of the band) matches the interpolated value at $0.981 \mu\text{m}$ (left shoulder of the band)

Additional features, detectable for selected moons, are the $3.1 \mu\text{m}$ Fresnel peak of water ice seen on Janus and possibly Methone, and the faint $1.25 \mu\text{m}$ water ice absorption seen on Atlas, Pan, Prometheus and possibly also Pandora and Methone. Apart from water ice, no evidence of other volatiles is seen, including CO_2 with its diagnostic feature at $4.26 \mu\text{m}$ (e.g., Chaban et al. 2007), although this falls in a rather noisy spectral region (Buratti et al. 2019).

Interestingly, Pan, Daphnis, and Atlas (orbiting within and in close proximity to the A ring, respectively), appear to group separately in terms of spectral shape from the co-orbital Janus and Epimetheus (orbiting at larger heliocentric distances between the F ring and Mimas), with the former being characterized by larger UV absorption and water ice band depths, and a smaller NIR spectral slope, suggesting a link with radial distance. Given this, one might expect that Prometheus and Pandora, orbiting just inside and outside the F ring, might share similar spectral shapes. However this is not the case, with Prometheus' spectrum being relatively similar to Atlas' and Pan's, while Pandora displays a distinctively smaller UV absorption.

This is better appreciated by comparing spectral indicators across the different ring moons, which we put here in a broader context with Saturn's main rings and mid-sized

inner moons (plus their Lagrangian satellites). The suite of VIMS spectral indicators we consider are (see Filacchione et al. 2010, 2012, 2013, for further details):

- the spectral slope of the target's full-disk I/F spectrum normalized at 0.55 μm , from a linear best-fit in the 0.35-0.55 μm range: referred to as the UV-VIS slope;
- the spectral slope of the target spectrum normalized at 0.55 μm , from a linear best-fit in the 0.55-0.95 μm range: referred to as the VIS-NIR slope;
- the band depth of the 1.5- μm water ice absorption: $\text{BD}_{1.5 \mu\text{m}}$;
- the band depth of the 2- μm water ice absorption: $\text{BD}_{2 \mu\text{m}}$.

The UV-VIS and VIS-NIR slopes are proxies for the level of contaminants and chromophores mixed with the water ice (Clark et al. 2012; Ciarniello et al. 2021), while the $\text{BD}_{1.5 \mu\text{m}}$ and $\text{BD}_{2 \mu\text{m}}$ are sensitive to both the water ice grain size (Clark and Lucey 1984; Stephan et al. 2021) and the level of contaminants (Ciarniello et al. 2021). Furthermore, we integrate this information with indicators derived from ISS observations of Saturn's icy moons, namely the brightness coefficient at 650 nm (Hedman et al. 2020, and Sect. 6.1), a proxy for the amount of dark contaminants mixed with water ice, and the GRN/UV3 and IR3/GRN color filter ratios, analogues of the UV-VIS and VIS-NIR slopes from VIMS. These brightness ratios are derived from sets of calibrated images obtained through the relevant filters at nearly the same time and viewing geometry. We simply compute the integrated brightness of the moon (I/F) for each image in the set, and plot the ratios of the appropriate integrated brightness estimates. Scatter plots from different combinations of VIMS and ISS spectral indicators are shown in Figs. 5 and 6.

The $\text{BD}_{1.5 \mu\text{m}}$ vs. $\text{BD}_{2 \mu\text{m}}$ scatter plot (Fig. 5) shows that the water ice band depths of both main rings and inner moons are strongly correlated, with the corresponding values aligning along two partially overlapping diagonal branches, extending from small to high values of the two indicators. This is consistent with differences in water ice grain size and/or amount of contaminants (darkening materials) among the different targets, as these properties affect the $\text{BD}_{1.5 \mu\text{m}}$ and $\text{BD}_{2 \mu\text{m}}$ in a similar way. Along the icy moon branch, the ring moons (except Methone) populate the extremal positions, with Pan and Prometheus displaying the deepest water ice absorptions, and Janus and Epimetheus the lowest. The mid-sized icy moons and the lagrangian satellites populate the part of the branch at intermediate values. Along the main ring branch, the lowest values are registered for the C ring, falling below Janus and Epimetheus, while the largest band depths occur in the A and B rings, similar to Pan and Prometheus. In order to discern whether the $\text{BD}_{1.5 \mu\text{m}}$ - $\text{BD}_{2 \mu\text{m}}$ correlation is primarily driven by a variation of 1) the regolith grain size or of 2) the amount of darkening contaminants among the different targets, we can take into account also their albedo.

This is addressed in the brightness coefficient (B) vs. $\text{BD}_{2 \mu\text{m}}$ scatter plot (Fig. 6). Here, the mid-sized icy moons with the Lagrangian satellites and the ring moons tend to distribute along two separate branches, where B and $\text{BD}_{2 \mu\text{m}}$ are positively correlated. This would be consistent with variations primarily due to the amount of contaminants, whose increasing abundance simultaneously reduces the 2- μm band depth and the brightness coefficient along the two branches.⁶ In this respect, the ring moons, being on average darker than the mid-sized icy moons and Lagrangian satellites, are likely to host larger amounts of contaminants

⁶Notice that a simultaneous reduction of the 2- μm band depth and visible reflectance can be also consistent with the effect of increasing grain size, in the case of coarse water ice regolith. This would require grains larger than a few hundreds of microns (Stephan et al. 2021), for which the 2- μm band starts saturating. However, the typical estimated water ice grain sizes of Saturn's icy moons and main rings are generally (much) smaller (Cuzzi et al. 2009; Bradley et al. 2010; Ciarniello et al. 2011; Filacchione et al. 2012; Clark et al. 2012; Bradley et al. 2013; Cuzzi et al. 2018b).

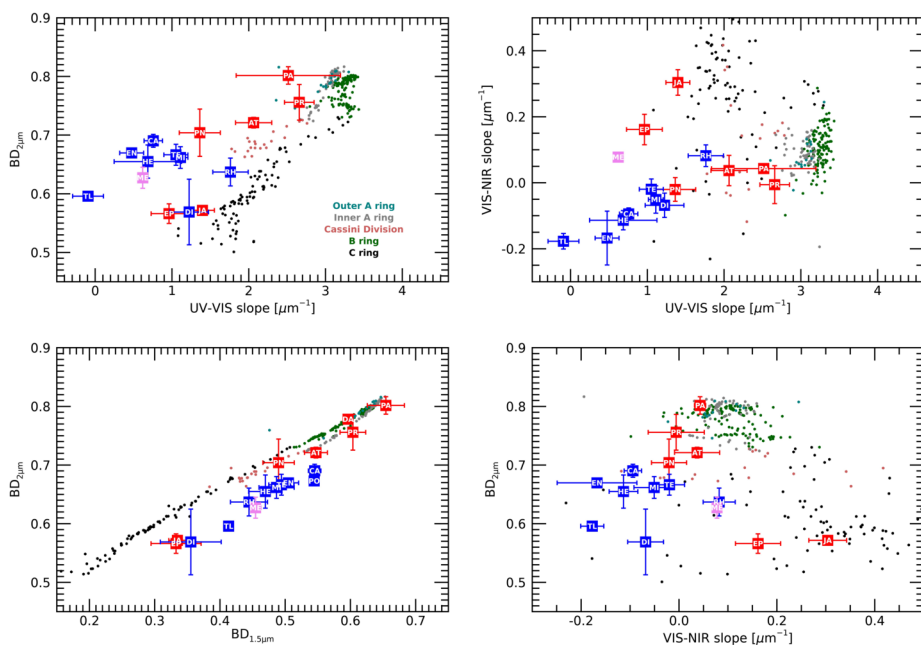


Fig. 5 Scatter plots of available VIMS spectral indicators for Saturn's ring moons (red symbols and pink for Methone), mid-sized icy moons with Lagrangian satellites (blue), and main rings (dots). Main ring spectral indicators are from a ring radial spectrogram⁷ with 200-km resolution, built from the VIMS' radial mosaic observation sequence S36-SUBML001 acquired on 19 December 2007 (Filacchione et al. 2014). Spectral indicators of the moons are computed from VIMS full-disk reflectance data after photometric correction to 50° phase angle; a similar photometric correction has been applied also to main ring data (See Appendix A). UV-VIS and VIS-NIR slopes for Methone are from ISS data (see Fig. 4). Abbreviations: Pan (PA), Daphnis (DA), Atlas (AT), Prometheus (PR), Pandora (PN), Epimetheus (EP), Janus (JA), Mimas (MI), Methone (ME), Enceladus (EN), Tethys (TE), Telesto (TL), Calypso (CA), Dione (DI), Helene (HE), Polydeuces (PO)⁸, and Rhea (RH)

on their surfaces. The existence of two branches, with the E-ring moons having a smaller band depth than ring moons with similar brightness coefficient, might also indicate that the former have a smaller characteristic regolith grain size, consistent with accumulation on their surfaces of fine water ice particles from the E ring. A similar argument, based on differences in the abundance of darkening contaminant(s), can be applied also for the main rings, where the A and B rings, intrinsically brighter than the C ring (Cuzzi et al. 2018b; Ciarniello et al. 2019), display larger water ice band depths.

In the UV-VIS slope vs. $BD_{2\mu m}$ scatter plot (Fig. 5), the different targets tend to globally align along a relatively broad diagonal distribution, with larger band depths corresponding to larger slopes. Nonetheless, different classes of object tends to cluster separately. The main rings populate a diagonal branch shifted to higher spectral slopes with respect to the inner

⁷Radial spectrograms are bi-dimensional arrays reporting the spectrum of the rings at different radial distances, sampled along a regular grid (Filacchione et al. 2012). The spectrum at a given position of the grid is obtained by averaging spectra of pixels falling in a given radial distance bin, acquired during a given VIMS radial mosaic observation.

⁸For Polydeuces only one VIMS IR sub-pixel observation was available at a relatively large phase angle of 120°, for which no photometric corrections has been applied.

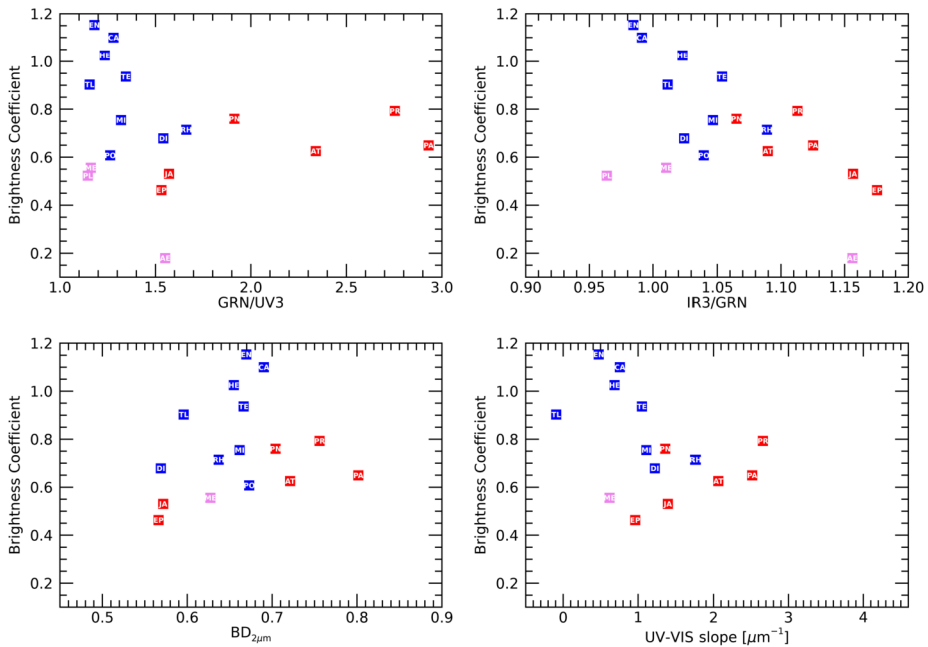
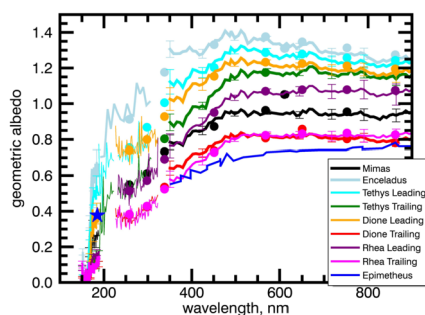


Fig. 6 Scatter plots of available VIMS and ISS spectral indicators for Saturn's ring moons (red symbols and pink for the ring-embedded moons Aegaeon, Methone, and Pallene) and mid-sized icy moons with Lagrangian satellites (blue). The brightness coefficient is derived from ISS clear filter observations (650 nm) reported at 30° phase angle, while color ratios are computed at 50° . The UV-VIS slope and $BD_{2\mu m}$ are from VIMS full-disk reflectance observations after photometric correction to 50° phase angle (See Appendix A). The UV-VIS slope for Methone is from ISS data (see Fig. 4). Abbreviations: Pan (PA), Daphnis (DA), Atlas (AT), Prometheus (PR), Pandora (PN), Epimetheus (EP), Janus (JA), Mimas (MI), Aegaeon (AE), Methone (ME), Pallene (PA), Enceladus (EN), Tethys (TE), Telesto (TL), Calypso (CA), Dione (DI), Helene (HE), Polydeuces (PO), and Rhea (RH)

moons, with the A and B rings having the largest slopes and band depths. The ring moons (except Methone) span a similar region of the scatter-plot, but shifted at slightly smaller UV-VIS slope values for similar $BD_{2\mu m}$. As such, they appear as a transition population between the main rings and the inner mid-sized moons plus their Lagrangian satellites, which, with the exception of Rhea and Dione, and including Methone, are located in a portion of the scatter plot at even smaller spectral slope. The overall positive correlation of the UV-VIS slope and $BD_{2\mu m}$ for the main rings and ring moons would support the idea that the contaminant(s) providing the UV absorption for these targets is likely embedded in the water ice grains (Nicholson et al. 2008; Ciarniello et al. 2011; Hedman et al. 2013; Cuzzi et al. 2018b; Ciarniello et al. 2019). The UV-absorber would be different from the broad-band absorber which reduces the overall albedo and spectral contrast (see above).

This interpretation would be consistent with the distributions of the ring moons (excluding the ring-embedded moons) in the B vs GRN/UV3 scatter plot (Fig. 6), aligning along a branch over which the two indicators are positively correlated. This simple paradigm, however, might not apply to the E-ring moons, which do not display a clear correlation between the UV-VIS slope and $BD_{2\mu m}$, and are aligned along a different branch in the B vs GRN/UV3 plot, where these quantities are roughly anti-correlated. Notice that similar considerations are also supported from the B vs UV-VIS slope scatter plot (Fig. 6), consistent

Fig. 7 UV-visible spectrum of Epimetheus compared with the inner icy moons of Saturn (Mimas, Enceladus, Tethys, Dione, Rhea). Epimetheus composite spectrum uses data from Cassini VIMS and UVIS (single point at 185 nm). Inner icy moons composite spectra use data from Cassini UVIS, ISS, VIMS and HST (after Hendrix et al. 2018)



with the B vs GRN/UV3 plot, as expected. This also appears in agreement with UVIS data (Buratti et al. 2019) of Epimetheus; Epimetheus was the only of the small satellites with adequate-enough signal-to-noise for UVIS to determine a reflectance value at 185 nm. This value is compared with the Epimetheus spectrum from VIMS and similar UVIS-ISS-VIMS and Hubble Space Telescope (HST) composite spectra for the mid-sized moons (Fig. 7) to demonstrate that Epimetheus, while having a lower albedo than most of the mid-sized moons at visible wavelengths, also displays a shallower UV absorption in the 300–400 nm region. This is a different trend than seen among the mid-sized moons, where lower albedo surfaces are correlated with a deeper UV absorption (Hendrix et al. 2018).

Ring moons (except Methone) separate the E-ring moons and main rings also in the UV-VIS slope vs. VIS-NIR slope scatter plot. The main rings distribute roughly along a diagonal branch where the VIS-NIR slope and UV-VIS slope are anticorrelated, and which is broadly aligned with a similar ring moon branch, although shifted at both smaller VIS-NIR slope and UV-VIS slope values. Instead, the E-ring moons, align along a diagonal branch where the VIS-NIR slope and UV-VIS slope are positively correlated, orthogonal to the ring moon and main ring distributions. This would be consistent with a single contaminant providing both the UV absorption and VIS-NIR coloring on the moons populating the E ring, while, as suggested above, for the ring moons and main rings two separate contaminants, a UV and a broad band absorber, can be envisaged (Cuzzi and Estrada 1998; Hedman et al. 2013; Cuzzi et al. 2018b; Ciarniello et al. 2019).

A similar grouping of the different targets, as in the VIS-NIR slope vs. UV-VIS slope and UV-VIS slope vs. $BD_{2\mu m}$ cases, can be observed in the VIS-NIR slope vs. $BD_{2\mu m}$ scatter plot (Fig. 5). The main rings and ring moons (except Methone) populate roughly parallel branches where VIS-NIR slope vs. $BD_{2\mu m}$ are anticorrelated, with the ring moons shifted at slightly smaller values of VIS-NIR slope. This population separates the main rings from the E-ring moons, which tend to cluster at smaller VIS-NIR slope and $BD_{2\mu m}$ values. For the main rings and ring moons (except Methone), this would be consistent with the effect of a broad-band absorber mixed with water ice, simultaneously reducing the spectral contrast of the water ice absorption features and reddening the otherwise neutral-to-blue VIS-NIR spectrum. This is also consistent with Fig. 6, where for the inner ring moons B increases at decreasing IR3/GRN. A similar trend is also observed for the largest E-ring moons, and roughly for the ring-embedded moons.

6.3 Clues from Spectral Modeling of the Rings and Mid-Sized Icy Moons

Extensive spectral modeling efforts of the UV-VIS-IR observations of the main rings (Cuzzi and Estrada 1998; Poulet et al. 2003; Bradley et al. 2010; Hedman et al. 2013; Cuzzi et al.

2018b; Ciarniello et al. 2019) and the mid-size icy moons (Ciarniello et al. 2011; Clark et al. 2012; Filacchione et al. 2012) have been made using regolith radiative transfer theories developed by Shkuratov et al. (1999, 2005, 2012) and Hapke (2012). The goal has been to test compositional paradigms for the surfaces of these targets, primarily to characterize the nature and amount of contaminants mixed with the water ice. For the ring moons, a similar approach has been attempted so far only for VIMS data on Epimetheus by Buratti et al. (2010), which suggested that its VIS-IR spectrum can be modeled with an intimate mixture of water ice and $\sim 5\%$ of Triton tholin,⁹ the latter being responsible for the UV absorption and the reddish VIS-NIR spectral slope (Khare et al. 1994). Small amounts ($<1\%$) of Titan tholins (Imanaka et al. 2004, 2012; West et al. 2014) have been invoked in spectral modeling of the main rings as a UV absorber embedded in water ice grains (known as an intramixture), along with an additional contaminant to provide broad-band absorption, either in pure form (e.g. carbon, silicates), or embedded in water ice (carbon, silicates, iron-rich phases) (see Hedman et al. 2013; Cuzzi et al. 2018b; Ciarniello et al. 2019; Miller et al. 2024, this collection).

Simulations fitting the main ring spectra require increasing amounts of a broad-band absorber moving from the intrinsically brighter A and B rings to the darker C ring and Cassini Division (Cuzzi et al. 2018b; Ciarniello et al. 2019). This simultaneously reduces the overall albedo, mutes the spectral contrast of the water ice bands and UV absorption, and reddens the spectrum at VIS-NIR wavelengths. This is consistent with the trends of Fig. 5, where, for the main rings, the UV-VIS slope is (i) larger for the A and B rings than for the C ring and Cassini Division; (ii) increases with $BD_{2\mu m}$; and (iii) decreases with increasing VIS-NIR slope.

The ring moons display spectral shapes similar to the main rings and are distributed in the spectral indicator scatter plots along branches roughly parallel to those of the rings. Furthermore, the albedo of the ring moons is correlated with UV-VIS slope and $BD_{2\mu m}$ and anticorrelated with VIS-NIR slope (Fig. 6). This suggests that the ring moons share a similar surface composition with the main rings, and that the abundance of the broad-band absorber is a driver of the observed spectral variability, affecting ring moons and main rings in a similar way. In this respect, increasing amounts of such a spectrally bland contaminant, which would determine the spectral transition from the bright and reddish (in the UV-VIS region) A and B rings to the dark and less-red C ring (Cuzzi et al. 2018b), might also explain the spectral differences in moving from the inner ring moons (Pan, Daphnis, Atlas, Prometheus and Pandora) towards the co-orbital moons (Janus and Epimetheus).

Spectral models based on water-ice grains containing small ($\leq 0.4\%$) amounts of tholin (to provide the UV absorption), intimately mixed with a variable fraction of amorphous carbon (acting as a broad-band absorber), have been employed to fit the UV-NIR spectra of the mid-sized icy moons orbiting within the E-ring, Mimas, Enceladus, Tethys, Dione, Rhea (Ciarniello et al. 2011; Filacchione et al. 2012). However, the observed positive correlation of the UV-VIS slope and VIS-NIR slope slopes, both inversely correlated with the brightness coefficient B , cannot be explained solely in terms of variations in the abundance of a broad-band absorber. This likely points to a role of nearly pure water ice grains from the E ring (Hendrix et al. 2018; Hedman et al. 2020), limiting the usefulness of a comparison between the ring moons and icy satellites embedded in the E-ring.

An alternative compositional paradigm suggested by Clark et al. (2012) posits that the spectral signatures of the darkening materials in the Saturn system are dominated by iron-rich compounds (nano-phase iron and nano-phase iron oxide). Spectral models including

⁹Tholins are a wide class of macro-molecular organic compounds obtained from irradiation of simple carbon-bearing materials such as CH_4 , C_2H_6 , in presence of N_2 or H_2O (Khare et al. 1984; McDonald et al. 1994).

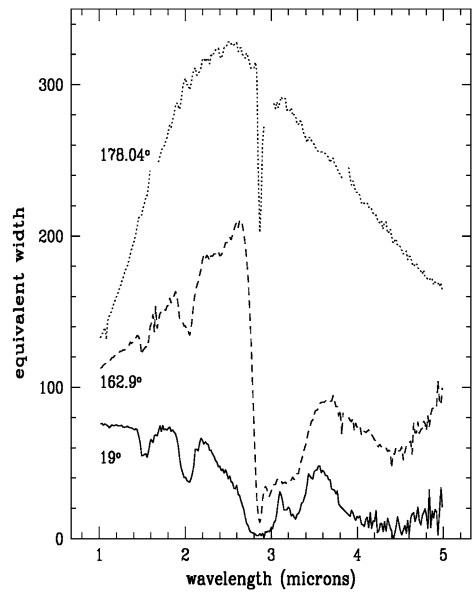
complex mixtures of variable amounts of these materials, water ice, and CO₂ provide good fits to the different terrains on Iapetus (bright, intermediate, and dark), Phoebe, Hyperion (dark and bright materials), Dione and the F ring. Clark et al. (2012) point out the similarity between the spectrum of Iapetus's bright material with the Cassini Division and C ring, and that of Hyperion with Epimetheus.

This might suggest that iron-rich compounds could also explain the VIS-NIR spectral variability among the main rings and ring moons. However, from a quantitative perspective, the A and B rings and the inner ring moons out to Prometheus are much redder (i.e., display a larger UV absorption; Filacchione et al. 2012) and brighter than are the Iapetus (Blackburn et al. 2011) and Hyperion (Thomas et al. 2007) bright materials (the reddest among the ones modeled in Clark et al. 2012). Thus it remains an open question whether models including iron-rich contaminants as darkening and UV-absorbing materials would be able to match the spectral properties of these targets.

Ongoing work (Hendrix et al. 2022) to simulate the UV-visible spectrum of the dark leading hemisphere of Iapetus shows that spectral models including carbon-rich tholins appear to better match the spectral shape of Iapetus, compared with models that consider irons only (with no tholins). This suggests that the tholin-based compositional paradigm might have the potential to explain the entire range of spectral variability from the brighter/redder to darker/less red rings and ringmoons.

A quantitative comparison between the physical and compositional properties of rings and ring moons would require conducting a systematic effort of regolith radiative transfer (RRT) modeling on available spectral observations of the latter. Ring moon RRT models would face similar difficulties as those encountered in ring modeling which we briefly address here (see a complete discussion of spectral modeling caveats in Sect. 4.1 of Miller et al. 2024, this collection). In this respect, whereas the mixing modality of the UV absorber, and tholin in particular, as embedded in water ice grains (intramixture) appears as a fairly consistent result from ring models (Poulet et al. 2003; Cuzzi et al. 2018b; Ciarniello et al. 2019), this is not the same for the neutral absorber. Recent ring models of Cuzzi et al. (2018b) and Ciarniello et al. (2019) provide reasonable fits of the UV-VIS spectral properties of the main rings, by including the neutral absorbers using different mixing modalities, that is as embedded in water ice grains or in a “salt-and-pepper” fashion (intimate mixture). Intramixtures with water ice maximize the absorbing power of the non-icy materials, making it proportional to their mass fraction, and typically requiring smaller abundances of contaminants with respect to intimate mixtures. Furthermore, pure grains of highly absorbing materials, as neutral absorbers in intimate mixtures, might turn completely opaque if larger than a given grain size, thus suppressing any grain-size dependency on the corresponding spectral properties. In this regime, the absorbing power becomes proportional to the total cross-section of the contaminant, implying that larger grains have the same darkening power (same total cross-section) of smaller ones, but with larger total mass fraction. All this implies that the inferred fraction of contaminants from spectral modeling strongly depends on the chosen mixing modality. An additional complication is represented by the shadowing induced by macroscopic surface roughness, both affecting ring particles and ring moons. Rougher surfaces would have larger contributions from shadows, thus reducing the total amount of scattered light. This is reflected in a reduction of the surface Bond albedo of the ring particles and ring moons (Cuzzi et al. 2017, 2018b), which, if not accounted for, can be erroneously interpreted in terms of larger abundances of non-icy contaminants when RRT is performed. Such aspects become particularly relevant if the absolute values of the inferred amounts of non-icy materials are used to constrain the effectiveness of contamination processes among these. For example, following these arguments and adopting

Fig. 8 Infrared spectra of the F-ring equivalent width at phase angles 178.04° , 162.9° , and 19° from VIMS observations. The equivalent width is computed as the radial integral of the ring brightness. The spectra at lower phase angles clearly display the 1.5-, 2- and 3- μm water ice bands. The high phase angle spectrum (178.04°) shows the Christiansen feature at $2.8 \mu\text{m}$. The spectra at 178.04° and 9° have been scaled down by a factor of 9 and 30, respectively. From Vahidinia et al. (2011)



an intra-particle mixing paradigm as in recent RRT modeling of the main rings, we might expect that the only available estimation of the tholin fraction for a ring moon (Epimetheus; Buratti et al. 2010) might be revised towards smaller abundances, possibly closer to main ring values.

7 Composition of the F-Ring and G-Ring

Outside of the main rings are a variety of dusty rings, the three most prominent being the F, G and E rings. At the moment, we have the most compositional information about the E ring thanks to the extensive data obtained by Cassini's Cosmic Dust Analyzer (Srama et al. 2004), which directly sampled particles within this ring and Enceladus' plume. These data reveal that the majority of particles in the E ring are composed primarily of water ice, consistent with near-infrared spectral data. However, some of the particles in this ring were also found to contain organics, salts and silicates (Postberg et al. 2009, 2011; Hsu et al. 2015; Postberg et al. 2018).

By contrast, information about the compositions of the F and G rings is much more limited because these rings were considered too hazardous for Cassini to fly through and directly sample. Furthermore, since the visible particles in these rings are extremely small (around 1-100 microns), their spectral and photometric properties are more sensitive to the particle size distribution and structure than to composition, because diagnostic absorption bands are strongly suppressed.

Despite these limitations, the remote sensing data do provide some useful constraints on the composition of the F ring, which is a relatively bright ring and so multiple high signal-to-noise visible and near-infrared spectra were obtained by VIMS (Clark et al. 2008; Vahidinia et al. 2011). Infrared spectra obtained at low to moderate phase angles show all the standard signatures of water ice (Fig. 8). There is also a decrease in brightness shortwards of $0.5 \mu\text{m}$ that might be due to the same UV absorption seen in the main rings and moons, but

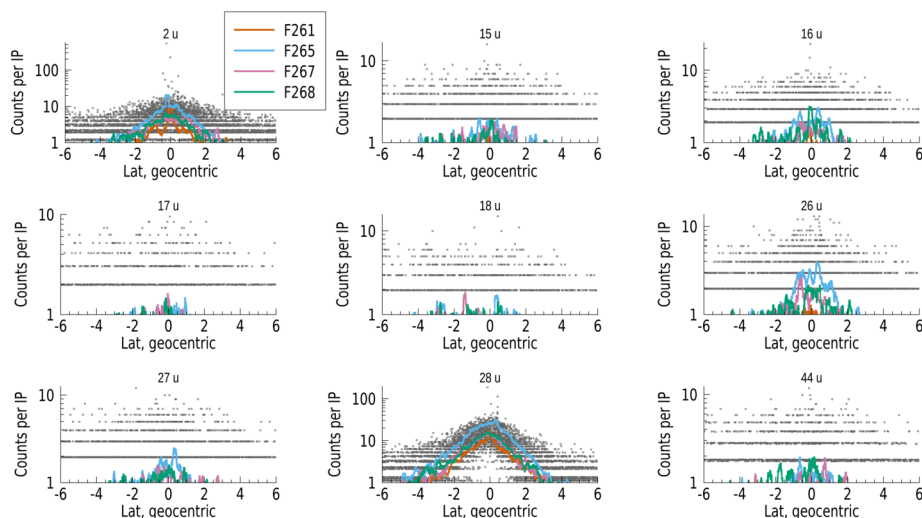


Fig. 9 In situ data from INMS during orbits near the F ring reveal the presence of icy grains. Grey points are individual datapoints from the four passes, and the overplotted lines show the smoothed data

the interpretation of this feature is complicated by a broad brightness peak centered around $0.5 \mu\text{m}$ likely due to a relatively high fraction of sub-micron grains (Clark et al. 2012).

Meanwhile, observations at extremely high phase angles (Fig. 8) show a strong dip near $2.8 \mu\text{m}$ which corresponds to the Christiansen frequency of crystalline water ice (Vahidinia et al. 2011; Hedman et al. 2011). This spectral feature arises at wavelengths where the real refractive index of the material approaches 1, which greatly reduces the scattering efficiency in these geometries. Since only water-ice is known to have a real refractive index near 1 at these wavelengths, this means that the F-ring particles need to be composed primarily of crystalline water ice like the rest of the rings.

By contrast, the signal-to-noise ratio of the available Cassini spectra of the G ring is very low, making even the comparatively strong $3 \mu\text{m}$ water ice absorption band difficult to quantify (although it does appear to be present). Robust constraints on the G ring's composition will therefore likely have to await future studies that co-add data from the entire span of the Cassini mission to obtain sufficiently high signal-to-noise spectra of this ring.

Additional compositional information about the F ring can be obtained from in situ data collected by the Ion and Neutral Mass Spectrometer (INMS Waite et al. 2004) in the closed source neutral mode during four orbits that crossed the ring plane outside of the F ring, shown in Fig. 9. The data are dominated by 2 u and 28 u. Signal at 2 u may be a mixture of water ion fragments and H_2 sourced from the main ring atmosphere (Tseng et al. 2011), with possible contributions from Enceladus (Jurac and Richardson 2007; Cassidy and Johnson 2010). However, the similar distributions for 2 u and 28 u support a common origin such as icy grains rather than gaseous material, which should show different scaleheights for the different masses (Perry et al. 2017). While the molecular water peak at 18 u and fragment peak at 17 u are relatively low, this may be related to the speed of the spacecraft. High velocity impacts of ice grains have been found to increase the measured 2 u to 18 u ratio, with titanium vapor produced from the INMS antechamber by the impacts likely scavenging the resulting oxygen (Walker et al. 2015). The 28 u peak is likely related to CO and/or oxidation at the filament of organic carbon. Note that data shown in Fig. 9 show counts per

IP, which are related to environmental density by a mass-dependent ram factor. This ram factor leads to nearly a factor of four apparent increase for 28 u as compared to 2 u.

The pattern of peak heights with 28 u > 26 u > 27 u may be associated with the presence of unsaturated organics with an O or N heteroatom. However, multiple different compounds may contribute to the signal, and no single compound was found to match the pattern. Some of these compounds also produce mass fragments at 15 and 16 u, and a further subset also produce fragments at 44 u. Masses associated with atomic H (1 u) and O₂ (32 u) were not part of the “closed source neutral” measurement sequence, and it is possible that 16 u may be associated with O₂ instead. While 32 u was measured in “open source ion” mode, without the enhancement from the closed source the signal is below detection limits.

8 Radial Variability of the Spectral Indicators and Exogenic Processes Affecting Surface Properties

Icy satellites in the Saturn's system are subject to a series of different exogenic processes affecting their surfaces, including contamination from ring material in the nearby A, F and E rings (Hendrix et al. 2018; Buratti et al. 2019; Hedman et al. 2020), the pollution from meteoritic dust (Cuzzi et al. 2009), and bombardment by charged particles (Roussos et al. 2008; Paranicas et al. 2018; Hedman et al. 2020). Concerning ring moons, these processes modify the composition of the ring material from which they accreted, to determine their surface composition and the resulting spectral properties we observe today. The magnitude of the effects of such exogenic processes on the different objects orbiting Saturn, including the main rings, depend primarily on the object position, and can be put in relation with radial spectral/albedo gradients in the system.

In Fig. 10 the spectral indicators from VIMS data (see Sect. 6.2: UV-VIS and VIS-IR slopes, BD_{1.5 μm}, and BD_{2 μm}) for the main rings and icy moons are reported as a function of the radial distance from Saturn. This complements, for the icy moons, the information of Fig. 3 reporting radial trends of the brightness coefficient, GRN/UV3 and IR3/GRN color ratios from ISS observations, and the relative fluxes of E-ring grains and high energy protons and electrons. Looking at Fig. 10, it can be noted that VIMS spectral indicators of the ring moons inside Mimas' orbit progressively approach A-ring values moving inward from Janus/Epimetheus to Pan, with an increase of the water ice band depths (BD_{1.5 μm} and BD_{2 μm}) and UV-VIS slope, and a reduction of the VIS-NIR slope, for which the trend is entirely driven by the particularly high values of Janus and Epimetheus. Such combined variation of the ring moon spectral indicators would appear consistent with a progressive enrichment with increasing radial distance of a broad-band-absorbing contaminant (see Sect. 6), resulting in a modification of the A-ring-like spectral properties of Pan/Atlas towards those of Janus/Epimetheus. It must be mentioned, however, that this picture is not fully consistent with the observed trend in the brightness coefficients (Fig. 3), with Prometheus and Pandora displaying the largest albedos among the ring moons. Furthermore, Prometheus sticks out from the expected radial trend also for what concerns the water ice band depths and the UV-VIS slope, displaying values larger than expected. This indicates that, at least for Prometheus and Pandora, an additional driver of the spectral properties should be considered.

Assuming that B and A rings preserve the least altered ring material (see Miller et al. 2024, this collection), and that their spectral properties (including the signature of the UV absorber, considered intrinsic to the ring system) are shared by the newly formed ring moons, the overall enrichment with radial distance of a broad-band absorber, can be naturally explained by contamination from bombardment of meteoritic dust (Cuzzi et al. 2009).

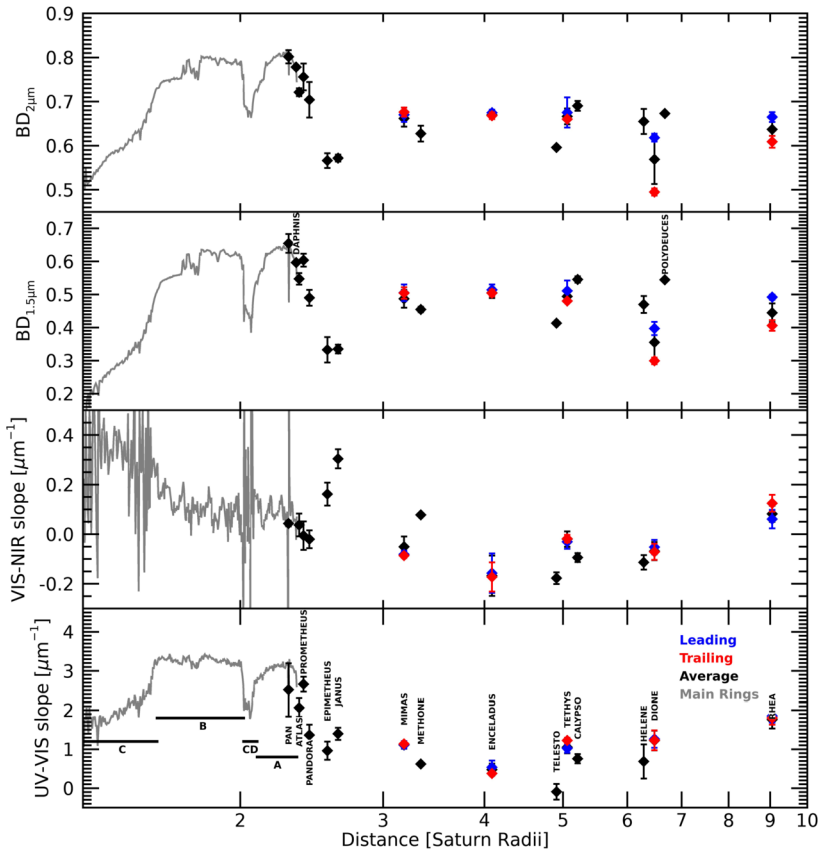
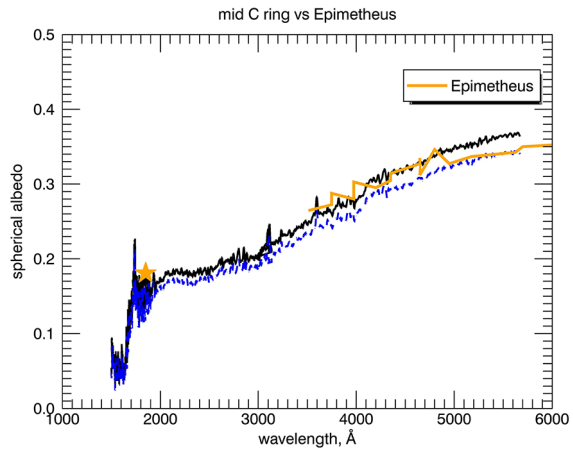


Fig. 10 Radial distribution of spectral indicators (UV-VIS and VIS-NIR slopes, $BD_{1.5\mu m}$, and $BD_{2\mu m}$) for Saturn's main ring (gray curves) and moons (diamonds) for which VIMS observations are available. Main ring values are derived from radial spectrograms with a 200-km radial sampling (see also Fig. 5). The respective radial extent of the different ring regions is indicated by horizontal bars (CD: Cassini Division). For Saturn's inner mid-sized moons (Mimas, Enceladus, Tethys, Dione, and Rhea) also leading and trailing hemisphere values are reported. UV-VIS slope and VIS-NIR slope slopes for Methone are from ISS data (see Fig. 4)

This would be consistent with the observed spectral properties of Janus and Epimetheus, possibly formed before the other inner ring moons (see Sect. 5), and then exposed for a longer time to such exogenous contamination. In this respect, it is interesting to note that their spectral indicators are similar to the C ring, where the contamination from the meteoritic flux is thought to be more effective than on the A and B rings (Cuzzi et al. 2018b; Ciarniello et al. 2019), because of the smaller optical depth (i. e. surface to mass ratio). Such similarity is confirmed by ultraviolet-visible composite spectra as shown in Fig. 11, with Epimetheus having a similar UV-visible spectral shape as the C ring. If so, the C ring on one side, and Janus/Epimetheus on the other, might represent the most contaminated endmembers for the main rings and inner ring moons, respectively.

An additional contribution affecting the surface composition of the ring moons inside Mimas' orbit and consistent with the observed spectral trends is the contamination from the nearby A ring particles. This would be more effective for ring moons close to the rings, and would contrast the effects of the meteoritic flux making the ring moon surface spectrally

Fig. 11 UV-visible spectrum of Epimetheus compared with a) the C ring. Epimetheus composite spectrum uses data from Cassini VIMS and UVIS (single point at 185 nm). C ring composite spectrum (black and blue curves) uses data from Cassini UVIS and Hubble Space Telescope Space Telescope Imaging Spectrograph (HST STIS) (after Cuzzi et al. 2018b)



more similar to the A ring (Buratti et al. 2019). Ring-related material is also lost by photo-ionization both into the planet and outwards beyond the rings into the magnetosphere. Photo-ionized molecules and atoms in the neutral ring atmosphere are accelerated in the magnetic field, and collide with neutrals of all species; this sends many of these large, but not yet charged, molecules beyond the edge of the rings at $2\text{--}3R_S$ and off into calmer regions of the magnetosphere where they may affect the surface properties of the inner moons. The loss rate is far larger near solstice than near equinox, by this process - a seasonal flow. In particular, near solstice, the column density of H_2 due to the rings in the magnetosphere out to perhaps $12R_S$, is only about 3 times smaller than the contribution due to Enceladus (Tseng et al. 2011; Tseng and Ip 2011) - that is, there is outward as well as inward mixing. The abundance of O_2 scattered outwards from the rings is only about an order of magnitude smaller than that contributed by Enceladus (Tseng et al. 2010, and see Miller et al. 2024, this collection, for further details). A quantitative treatment of mass exchange and associated compositional implications for the rings and inner ringmoons remains to be done.

Moving outward from Epimetheus/Janus orbits, along with the meteoritic dust flux, the two major processes affecting the icy moon surfaces are the contamination from E-ring grains and the bombardment by charged particles (Hendrix et al. 2018; Hedman et al. 2020). The effect of the surface accumulation of E-ring icy grains, originating from Enceladus' plumes, is likely responsible for the observed spectral trends among the mid-sized icy moons up to Janus and Epimetheus, with spectral slopes and color ratios increasing away from Enceladus, accompanied by a progressive reduction of the moons' visual albedo (Verbiscer et al. 2007; Hendrix et al. 2018; Hedman et al. 2020), in agreement with the decreasing modeled E-ring particle total flux (Fig. 3). E ring particles preferentially accumulate on the leading side of moons outside Enceladus' orbit, and on the trailing side for the inner ones. This is consistent with the observed visual albedo longitudinal asymmetries discussed in Sect. 6.1, and appear also in agreement with the distribution of the water ice band depths on Dione and Rhea, with values larger on their leading sides than on the trailing. The influence of high-energy particle fluxes on the surfaces of Saturn's moons is best demonstrated by the low surface brightnesses of the small moons Aegaeon, Methone and Pallene shown in Fig. 3. These three moons are all located within the inner flank of the E ring, but are significantly darker than one would predict based on the brightness trends observed among the larger moons Janus, Epimetheus, Mimas and Enceladus. The most likely explanation for the anomalously low brightnesses of these small moons is that they are exposed to a much higher

flux of high-energy protons. At suitably high energies, these protons are concentrated in a series of three belts that lie between the main rings and the orbits of Janus/Epimetheus, Mimas and Enceladus (Roussos et al. 2008; Paranicas et al. 2018). It turns out that those larger moons are efficient enough sinks for protons that they actually create localized depletions in the charged particle flux in their vicinity, while the smaller moons Aegaeon, Methone and Pallene are not such efficient proton sinks and so are exposed to much higher fluxes of charged particles. Furthermore, the brightnesses of all these moons are reasonably well correlated with the ratios of charged particle flux to E-ring particle flux experienced by each moon (Hedman et al. 2020). It is therefore reasonable to conclude that while E-ring particles can brighten the surfaces of Saturn's moons, high-energy charged particles like protons can somehow darken ice-rich surfaces.

At the moment, the physical mechanism by which the charged particles darken these moon's ice-rich surfaces is still unclear. In principle, the surfaces could become darker either due to changes in their chemistry or in the structure of their regoliths, but there are challenges with either of these interpretations. In particular, Methone has water ice band depths that are just slightly deeper than Mimas and Enceladus, so there is no indication that the radiation is causing significant changes in the structure of its regolith. At the same time, Methone has similar color ratios as Mimas and Enceladus, so there is also not any obvious compositional difference between these moons. The one potentially interesting spectral trend in this context are the strongly positive VIS-NIR slopes of Janus, Epimetheus, and Aegaeon. Such strong positive slopes are unusual for Saturn's moons, and while Janus/Epimetheus are not exposed to particularly high fluxes of high-energy protons, both Janus/Epimetheus and Aegaeon are exposed to high fluxes of moderately high-energy electrons (Roussos et al. 2008; Hedman et al. 2020).

As a final remark, we note that Hendrix et al. (2018) showed that connections could be made between the UV-visible spectral shapes of the mid-sized icy moons and the amount of E-ring grain and charged particle bombardment (namely the corotating plasma) experienced at the orbital locations of each moons. They suggested that the relatively low albedo of Rhea, and its relatively strong UV absorption, could be related to organics - emplaced by E-ring grain bombardment - on the surface, in combination with aging, via plasma bombardment-related weathering, of those E-ring organics. In this respect, Epimetheus' low albedo level and weak UV absorption (both smaller than Rhea's) do not appear fully consistent with the trend observed in the mid-sized icy moons (see Sect. 6.2), requiring further investigation.

9 Summary and Final Remarks

The surface composition of the inner ring moons, up to Janus and Epimetheus, as inferred from the UV-VIS-IR spectroscopic data of remote sensing instrument onboard the Cassini mission, appears linked to that of the main ring particles from which they accreted. This is supported by the overall observed spectral similarity between ring and ring moons and the similar trends of the spectral parameters (see Sect. 6 and Figs. 4 and 5), which suggests a common compositional paradigm. Nonetheless, the radial variability of the inner ring moon spectral properties can be also connected to the complex interplay of different exogenous processes affecting their surfaces. In this respect, the progressive departure from an A-ring like spectrum, moving from the innermost Pan to the outermost Janus/Epimetheus, can be interpreted in terms of a reduction with radial distance of the A-ring particle flux on the ring moon surfaces giving way to pollution from meteoritic dust. As mentioned above in Sect. 8, the similarity between Janus/Epimetheus surface composition and the C ring might

be interpreted as a result of a more effective pollution on these targets compared to the other ring moons and main rings, respectively. However, the occurrence of leading/trailing asymmetries on Janus and Epimetheus is likely the result of the accumulation of E-ring particle on these targets, and additional contamination might come from the nearby G-ring, fed by the low-albedo Aegeon. Also, the flux of energetic electrons is relatively large at Janus and Epimetheus orbital distance. These sources of exogenous material and the potentially darkening effect of energetic particles are only relevant for Janus and Epimetheus and not for the C ring. As such, the interpretation of the Janus/Epimetheus vs. C ring spectral similarity may not be straightforward as it would appear. In this respect, it is worth mentioning that Prometheus and Pandora, the ring moons with the largest albedo, possibly witness the effects of another source of exogenous material, represented by the accumulation of icy F-ring particles brightening their surfaces. Yet, Prometheus, being marginally brighter than Pandora, has significantly larger UV-slope and water ice band depths, which appears difficult to explain with the sole effect of F-ring grain accumulation. Further insights into the investigation of the compositional link between the main rings and the inner ring moons and the (different) exogenous processes affecting their surface spectrophotometric properties could be provided by complementing the results from the spectral indicator analysis with a systematic and quantitative comparison of their intrinsic albedos. In this respect, a key quantity to be compared would be the Bond albedo of the ring particles with that of the ring moons: this would allow us to overcome the bias encountered when comparing the reflectance of the main rings (a many-particle-thick layer, but with finite optical depth) with the reflectance of a ring moon surface (a semi-infinite optical depth medium). The Bond albedo of the main ring particles is starting to appear in the literature (Cuzzi et al. 2018b; Ciarniello et al. 2019), even if particle-surface shadowing effects have generally not been accounted for, while for the ring moons these albedos could be approximated by the brightness coefficient at a phase angle of $\sim 55^\circ$, computed following the approach of Hedman et al. (2020) (Sect. 6.1).

Ring-embedded moons (Aegeon, Methone, Anthe, and Pallene) appear as a separate class with respect to the rest of the ring moons and as such they would be less spectrally-linked to the main rings. Although, at the time of writing, there is limited hyperspectral information for this class of objects (namely only the IR spectrum of Methone), brightness coefficient vs color ratio scatter plots for Aegeon, Methone, and Pallene (Fig. 6) indicate they cluster separately from mid-sized icy moons and ring moons, displaying remarkably lower albedos with respect to satellites at comparable radial distance from Saturn. This is currently interpreted as a result of the relatively large fluxes of high-energy charged particles on their surfaces, dominating over the brightening effect of E-ring particle accumulation.

The comparison of ring moon spectral indicators with those of the mid-sized icy moons and their Lagrangian satellites reveal qualitatively different trends (Figs. 5 and 6). Notably, the UV absorption in ring moons is positively correlated with their surface brightness and water ice absorption band depths, and inversely correlated with the VIS-IR slope, supporting a compositional paradigm including at least two populations of grains, one of water ice particles with an embedded UV absorber (see Sect. 6.3 and references therein) and a second component providing a broad-band absorption. On the contrary, for the mid-sized icy moons and their Lagrangians the UV absorption is positively correlated with the VIS-IR slope while decreasing with the surface albedo, possibly pointing to a different compositional paradigm in which the same carrier might provide both the UV absorption and the surface darkening. This would be consistent with a scenario in which the average surface composition of these objects is primarily driven by the accumulated flux of E-ring particles (as evidenced by the albedo vs orbital distance trend), however assuming an aging of the E-ring particles due to exposure to radiolytic processes of their organic content, making them redder/darker.

As such, grains reaching mid-sized icy moons farther from Enceladus (as Rhea and Dione), would experience a longer radiolytic processing provide larger UV-reddening and darkening of their surfaces (Hendrix et al. 2018). However, Janus and Epimetheus, whose albedo leading/trailing hemisphere asymmetry suggests evidence of accumulation of E-ring grains on their surfaces and should receive larger fluxes than Rhea, do not seem to fit in this scenario, as they appear darker than Rhea while having a smaller UV-absorption. This points to a more complex picture, in which the resulting spectral properties of Janus and Epimetheus are the result of those inherited by the rings with superposition of the different exogenous mechanisms discussed above, including further processing of the organics in the E-ring particles accumulated on their surfaces by the relatively large fluxes of high energy electrons (Fig. 3), leading to carbonization which would progressively turn the grains from red to black.

In the current ring moon formation models these bodies could form 1) in the rings from original seeds, denser than the ring material, that may be shards from the destruction of a larger satellite or 2) at/near the Fluid Roche limit (outside the A ring) directly from ring material (Sect. 5). Disentangling between these two scenarios by means of compositional arguments based on spectroscopic observation does not appear as an easy task. The spectral similarity between main rings and ring moons, might just be representative of the ring moons outer layers, dominated by ring material, and hiding a potential inner seed not accessible by UV-VIS-IR spectroscopy. Furthermore, the evidence of a complex interplay of exogenous processes affecting the ring moon surfaces, as witnessed by the spectral radial trends, modifies the original composition inherited from the rings, to a degree which depends on the ring moon position and exposure time, i. e. its orbital evolution.

Once formed, embedded ring moons migrate outwards following the rings' viscous spreading, while isolated ring moons, emerged from the rings or formed just outside the FRL, are pushed by the one-sided ring torque. With the exception of Pan, orbiting inside the A ring, the ringmoon orbital evolution timescales, obtained by comparing the present distance from the A ring edge with the computed velocity of the outward radial drift, increase with the ringmoon radial distance, from $\sim 4 \times 10^6$ yr for Atlas, ~ 1 Gyr for Epimetheus (Sect. 5). Although it might be tempting to interpret these values as actual ringmoon ages, this is hindered by the fact the drift rate changes over time due to 1) the increase of the distance from the A ring, 2) possible (temporary) trapping in mean motion resonances with other satellites and, 3) variations in the ringmoon mass resulting from merging processes. These arguments appear even more relevant in the light of recent estimations of the age of Saturn's rings from the degree of pollution delivered by micrometeoroid infall (Kempf et al. 2023), posing an upper limit to ~ 400 Myr, which would be inconsistent with the above mentioned orbital evolution timescales (see also Crida et al. 2024, this collection). Nonetheless, these should still be meaningful in relative terms, and it appears broadly supported from a spectroscopic perspective, with Janus and Epimetheus, likely the oldest of the inner ring moons, being characterized by a more polluted appearance, possibly linked to a longer exposure to contamination processes.

The observed shapes of the inner ring moons may be either the result of ring material accretion onto the initial seed, which occurring preferentially at equatorial latitudes can also account for the equatorial ridge observed on Atlas, Pan, and Daphnis, or by a low-speed collision of two similar progenitors (Sect. 4). In the former case, one might hope to observe residual compositional differences between the ring moon central component and the equatorial ridge, if the internal seed is not completely hidden by the accumulated material. In this respect, Buratti et al. (2019) provided some information in terms of the disk-resolved ISS IR3/UV3 color ratio, as measured during the Cassini's ring-grazing orbits: for Pan and Atlas, the IR3/UV3 is 19% and 16% larger in the cratered terrains of their central

components than for their equatorial ridges, respectively. If the equatorial ridge is more representative of the ring material than the central component, and given that inner moons are typically redder possibly because of the larger ring particle influence, we might expect the equatorial ridge to be redder than the rest of the moon. However, it appears to be the opposite for Atlas and Pan, a somewhat puzzling result. Similar information is available also for Pandora, with a IR3/UV3 color ratio 15% lower in the craters than in the smooth equatorial material. This seems in line with the argument above, yet Pandora is in general much less red in the UV-VIS than the A ring and might be significantly influenced by F ring grains (which may be polluted like the low-optical depth portions of the main rings), thus it is not straightforward to interpret such variability as an effect of preferential main ring material accumulation at equatorial/intermediate latitudes. One way to distinguish observationally between the “ring material accretion at equatorial latitudes” and the “low-speed collision” scenarios would be to determine the rotational libration amplitude of these bodies in order to estimate their moments of inertia (Rambaux et al. 2022). In the first scenario, the body is heterogeneous (the solid internal seed plus less-dense ring material at the equator) while in the second case, the mixing would probably lead to a rather homogeneous body. The libration of small moons may be deduced directly from high-resolution images (Tiscareno et al. 2009) or indirectly using astrometric measurements of the periaapse variations (Lainey et al. 2019, 2023).

Despite the impressive wealth of data provided by the Cassini mission, tracing back the present compositional, morphological and orbital properties of the ring moons to the primordial phases of their formation in the rings endures as a difficult challenge. As summarized above, the series of processes modifying the surfaces of these bodies, and their dynamical evolution, are not fully unraveled yet, and will need to be quantitatively characterized by future theoretical and laboratory investigations. Hopefully, as recently achieved for the main rings, this will allow us to put independent and absolute constraints on the age of the ring moons and produce a more complete picture of how the Saturnian system evolved. Exploration of the Saturn system in the future might also allow us to sample the interior of the ring moons in the context of the nearby ring particles. This would pose crucial constraints on the formation processes and, by comparing surface and sub-surface properties, shed light on the exogenous mechanisms affecting these small satellites.

Appendix A: Photometric Correction of VIMS Data

VIMS full-disk spectra of Saturn's moons have been photometrically corrected to a reference phase angle of 50° before averaging procedures and computation of spectral indicators. This has been done by assuming that the icy moons spectrophotometric properties can be described by means of the Kaasalainen-Shkuratov model (Kaasalainen et al. 2001; Shkuratov et al. 2011), as discussed in Filacchione et al. (2022). This implies that the full-disk spectral reflectance of a given target ($FDR_\lambda(\alpha)$) after normalization at $0.55 \mu\text{m}$ can be expressed as

$$\frac{FDR_\lambda(\alpha)}{FDR_{0.55 \mu\text{m}}(\alpha)} = \frac{A_\lambda^{eq}(\alpha)}{A_{0.55 \mu\text{m}}^{eq}(\alpha)} \quad (\text{A.1})$$

where the subscript λ indicate different wavelengths, α is the phase angle and A^{eq} is the equigonal albedo. Given this, the normalized full-disk reflectance photometrically corrected at 50° can be expressed as

$$\frac{FDR_\lambda(50^\circ)}{FDR_{0.55 \mu\text{m}}(50^\circ)} = \left(\frac{FDR_\lambda(\alpha_0)}{FDR_{0.55 \mu\text{m}}(\alpha_0)} \right)_{VIMS} \frac{A_{0.55 \mu\text{m}}^{eq}(\alpha_0)}{A_\lambda^{eq}(\alpha_0)} \frac{A_\lambda^{eq}(\alpha)}{A_{0.55 \mu\text{m}}^{eq}(\alpha)} \quad (\text{A.2})$$

with $\left(\frac{FDR_{\lambda}(\alpha_0)}{FDR_{0.55\text{ }\mu\text{m}}(\alpha_0)}\right)_{VIMS}$ being the normalized full-disk reflectance spectrum from VIMS data. Filacchione et al. (2022) derived the equigonal albedos of Saturn's mid-sized inner moons (Mimas, Enceladus, Tethys, Dione, and Rhea) assuming a polynomial expression

$$A_{\lambda}^{eq}(g) = a_{0,\lambda} + a_{1,\lambda}(\alpha) + a_{2,\lambda}(\alpha)^2 \quad (\text{A.3})$$

with a set of different parameters $(a_{0,\lambda}, a_{1,\lambda}, a_{2,\lambda})$ for each target. Since spectrophotometric models for the rest of the Saturn's inner moons in the complete VIMS spectral range have not yet been derived at the time of writing, we perform the photometric correction of the observations of the different targets by means of Eq. (A.3), assuming for simplicity the set of parameters $(a_{0,\lambda}, a_{1,\lambda}, a_{2,\lambda})$ derived for the case of Rhea, with the exception of the mid-sized inner moons, for which the respective set of parameters were used.

With a similar approach, we also performed an empirical photometric correction of the main ring radial spectrogram presented in Sect. 6. This requires the simplifying assumptions that ring particles share spectrophotometric properties similar to the icy moons and that multiple scattering of light between ring particles is negligible. We judge this an acceptable approximation, considering the limited impact of the photometric correction for the main ring case, since the VIMS observations used to build the radial spectrogram were acquired with a phase angle of 38.8° , relatively close to the reference phase angle of 50° .

Acknowledgements This research was supported by the International Space Science Institute (ISSI) in Bern, through the ISSI Workshop “New Vision of the Saturnian System in the Context of a Highly Dissipative Saturn”. MC and GF acknowledge internal support from INAF-IAPS. KEM acknowledges internal support from SwRI. This work has made use of NASA's Astrophysics Data System. We thank P. Thomas for valuable comments and suggestions and two anonymous referees for helpful reviews that improved this article.

Author Contribution The idea for this review article came from GF and JC. All authors contributed to the literature search. New data analysis was performed by MC, FG, MMH, KEM, and AH. All authors contributed to drafting and revisions.

Funding Open access funding provided by Istituto Nazionale di Astrofisica within the CRUI-CARE Agreement. The project leading to this publication has received funding from the Excellence Initiative of Aix-Marseille Université–A*Midex, a French “Investissements d'Avenir program” AMX-21-IET-018. This research holds as part of the project FACOM (ANR-22-CE49-0005-01_ACT) and has benefited from a funding provided by l'Agence Nationale de la Recherche (ANR) under the Generic Call for Proposals 2022.

Data Availability Cassini data used in this work are archived in NASA's Planetary Data System (PDS).

Declarations

Competing Interests The authors have no competing interests to declare.

Open Access This article is licensed under a Creative Commons Attribution 4.0 International License, which permits use, sharing, adaptation, distribution and reproduction in any medium or format, as long as you give appropriate credit to the original author(s) and the source, provide a link to the Creative Commons licence, and indicate if changes were made. The images or other third party material in this article are included in the article's Creative Commons licence, unless indicated otherwise in a credit line to the material. If material is not included in the article's Creative Commons licence and your intended use is not permitted by statutory regulation or exceeds the permitted use, you will need to obtain permission directly from the copyright holder. To view a copy of this licence, visit <http://creativecommons.org/licenses/by/4.0/>.

References

- Asphaug E (2020) Interiors of small bodies and moons. *Nat Commun* 11:1564. <https://doi.org/10.1038/s41467-020-15458-8>
- Attree NO, Murray CD, Cooper NJ, et al (2012) Detection of low-velocity collisions in Saturn's F ring. *Astrophys J Lett* 755(2):L27. <https://doi.org/10.1088/2041-8205/755/2/L27>
- Beurle K, Murray CD, Williams GA, et al (2010) Direct evidence for gravitational instability and moonlet formation in Saturn's rings. *Astrophys J Lett* 718(2):L176–L180. <https://doi.org/10.1088/2041-8205/718/2/L176>
- Blackburn DG, Buratti BJ, Ulrich R (2011) A bolometric bond albedo map of iapetus: observations from Cassini vims and iss and Voyager iss. *Icarus* 212(1):329–338. <https://doi.org/10.1016/j.icarus.2010.12.022>
- Borderies N, Goldreich P, Tremaine S (1984) Unsolved problems in planetary ring dynamics. In: Greenberg R, Brahic A (eds) *Planetary rings*. University of Arizona Press, Tucson, pp 713–734
- Bradley ET, Colwell JE, Esposito LW, et al (2010) Far ultraviolet spectral properties of Saturn's rings from Cassini UVIS. *Icarus* 206(2):458–466. <https://doi.org/10.1016/j.icarus.2009.12.021>
- Bradley ET, Colwell JE, Esposito LW (2013) Scattering properties of Saturn's rings in the far ultraviolet from Cassini UVIS spectra. *Icarus* 225(1):726–739. <https://doi.org/10.1016/j.icarus.2013.04.008>
- Brown RH, Baines KH, Bellucci G, et al (2004) The Cassini Visual And Infrared Mapping Spectrometer (VIMS) investigation. *Space Sci Rev* 115(1–4):111–168. <https://doi.org/10.1007/s11214-004-1453-x>
- Buratti BJ, Bauer JM, Hicks MD, et al (2010) Cassini spectra and photometry 0.25–5.1 μm of the small inner satellites of Saturn. *Icarus* 206(2):524–536. <https://doi.org/10.1016/j.icarus.2009.08.015>
- Buratti BJ, Thomas PC, Roussos E, et al (2019) Close Cassini flybys of Saturn's ring moons Pan, Daphnis, Atlas, Pandora, and Epimetheus. *Science* 364:eaat2349. <https://doi.org/10.1126/science.aat2349>
- Burns JA, Showalter MR, Hamilton DP, et al (1999) The formation of Jupiter's faint rings. *Science* 284:1146. <https://doi.org/10.1126/science.284.5417.1146>
- Canup RM, Esposito LW (1995) Accretion in the Roche zone: coexistence of rings and ring moons. *Icarus* 113(2):331–352. <https://doi.org/10.1006/icar.1995.1026>
- Canup RM, Esposito LW (1996) Accretion of the Moon from an impact-generated disk. *Icarus* 119(2):427–446. <https://doi.org/10.1006/icar.1996.0028>
- Cassidy TA, Johnson RE (2010) Collisional spreading of Enceladus' neutral cloud. *Icarus* 209(2):696–703. <https://doi.org/10.1016/j.icarus.2010.04.010>
- Chaban GM, Bernstein M, Cruikshank DP (2007) Carbon dioxide on planetary bodies: theoretical and experimental studies of molecular complexes. *Icarus* 187(2):592–599. <https://doi.org/10.1016/j.icarus.2006.10.010>
- Chandrasekhar S (1969) *Ellipsoidal figures of equilibrium*. The Silliman Foundation lectures. Yale University Press, New Haven
- Charnoz S, Porco CC, Déau E, et al (2005) Cassini discovers a kinematic spiral ring around Saturn. *Science* 310(5752):1300–1304. <https://doi.org/10.1126/science.1119387>
- Charnoz S, Brahic A, Thomas PC, et al (2007) The equatorial ridges of pan and atlas: terminal accretionary ornaments? *Science* 318(5856):1622. <https://doi.org/10.1126/science.1148631>
- Charnoz S, Dones L, Esposito LW, et al (2009) Origin and evolution of Saturn's ring system. In: Dougherty MK, Esposito LW, Krimigis SM (eds) *Saturn from Cassini-Huygens*, p 537. https://doi.org/10.1007/978-1-4020-9217-6_17
- Charnoz S, Salmon J, Crida A (2010) The recent formation of Saturn's moonlets from viscous spreading of the main rings. *Nature* 465(7299):752–754. <https://doi.org/10.1038/nature09096>
- Charnoz S, Crida A, Castillo-Rogez JC, et al (2011) Accretion of Saturn's mid-sized moons during the viscous spreading of young massive rings: solving the paradox of silicate-poor rings versus silicate-rich moons. *Icarus* 216(2):535–550. <https://doi.org/10.1016/j.icarus.2011.09.017>. arXiv:1109.3360 [astro-ph.EP]
- Ciarniello M, Capaccioni F, Filacchione G, et al (2011) Hapke modeling of Rhea surface properties through Cassini-VIMS spectra. *Icarus* 214(2):541–555. <https://doi.org/10.1016/j.icarus.2011.05.010>
- Ciarniello M, Filacchione G, D'Aversa E, et al (2019) Cassini-VIMS observations of Saturn's main rings: II. A spectrophotometric study by means of Monte Carlo ray-tracing and Hapke's theory. *Icarus* 317:242–265. <https://doi.org/10.1016/j.icarus.2018.07.010>
- Ciarniello M, Moroz LV, Poch O, et al (2021) VIS-IR spectroscopy of mixtures of water ice, organic matter, and opaque mineral in support of small body remote sensing observations. *Minerals* 11(11):1222. <https://doi.org/10.3390/min11111222>
- Clark RN, Lucey PG (1984) Spectral properties of ice-particulate mixtures and implications for remote sensing. I. Intimate mixtures. *J Geophys Res* 89:6341–6348. <https://doi.org/10.1029/JB089iB07p06341>
- Clark RN, Curchin JM, Jaumann R, et al (2008) Compositional mapping of Saturn's satellite Dione with Cassini VIMS and implications of dark material in the Saturn system. *Icarus* 193(2):372–386. <https://doi.org/10.1016/j.icarus.2007.08.035>

- Clark RN, Cruikshank DP, Jaumann R, et al (2012) The surface composition of Iapetus: mapping results from Cassini VIMS. *Icarus* 218(2):831–860. <https://doi.org/10.1016/j.icarus.2012.01.008>
- Colwell JE, Nicholson PD, Tiscareno MS, et al (2009) The structure of Saturn's rings. In: Dougherty MK, Esposito LW, Krimigis SM (eds) *Saturn from Cassini-Huygens*. Springer, Dordrecht, pp 375–412. https://doi.org/10.1007/978-1-4020-9217-6_13
- Cooper NJ, Murray CD, Evans MW, et al (2008) Astrometry and dynamics of Anthe (S/2007 S 4), a new satellite of Saturn. *Icarus* 195(2):765–777. <https://doi.org/10.1016/j.icarus.2008.01.006>
- Cooper NJ, Renner S, Murray CD, et al (2015) Saturn's inner satellites: orbits, masses, and the chaotic motion of atlas from new Cassini imaging observations. *Astron J* 149(1):27. <https://doi.org/10.1088/0004-6256/149/1/27>. arXiv:1406.6492 [astro-ph.EP]
- Crida A, Charnoz S (2012) Formation of regular satellites from ancient massive rings in the Solar System. *Science* 338(6111):1196. <https://doi.org/10.1126/science.1226477>. arXiv:1301.3808 [astro-ph.EP]
- Crida A, Papaloizou JCB, Rein H, et al (2010) Migration of a moonlet in a ring of solid particles: theory and application to Saturn's propellers. *Astron J* 140(4):944–953. <https://doi.org/10.1088/0004-6256/140/4/944>. arXiv:1006.1573 [astro-ph.EP]
- Crida A, Estrada PR, Nicholson PD, et al (2024) The age and origin of Saturn's rings. *Space Sci Rev*
- Cuzzi JN (2024) Corrigendum to "Saturn's F ring core: calm in the midst of chaos" [*Icarus* 232 (April) (2014) 157–175]. *Icarus* 413:116011. <https://doi.org/10.1016/j.icarus.2024.116011>
- Cuzzi JN, Estrada PR (1998) Compositional evolution of Saturn's rings due to meteoroid bombardment. *Icarus* 132(1):1–35. <https://doi.org/10.1006/icar.1997.5863>
- Cuzzi J, Clark R, Filacchione G, et al (2009) Ring particle composition and size distribution. In: Dougherty MK, Esposito LW, Krimigis SM (eds) *Saturn from Cassini-Huygens*. Springer, Dordrecht, pp 459–509. https://doi.org/10.1007/978-1-4020-9217-6_15
- Cuzzi JN, Chambers LB, Hendrix AR (2017) Rough surfaces: is the dark stuff just shadow?: who knows what evil lurks in the hearts of men? The shadow knows! *Icarus* 289:281–294. <https://doi.org/10.1016/j.icarus.2016.10.018>
- Cuzzi JN, Filacchione G, Marouf EA (2018a) The rings of Saturn. In: Tiscareno MS, Murray CD (eds) *Planetary ring systems. Properties, structure, and evolution*. Cambridge University Press, Cambridge, pp 51–92. <https://doi.org/10.1017/9781316286791.003>
- Cuzzi JN, French RG, Hendrix AR, et al (2018b) HST-STIS spectra and the redness of Saturn's rings. *Icarus* 309:363–388. <https://doi.org/10.1016/j.icarus.2018.02.025>
- Cuzzi JN, Marouf EA, French RG, et al (2024) Saturn's F ring is intermittently shepherded by Prometheus. *Sci Adv*. <https://doi.org/10.1126/sciadv.adl6601> [astro-ph.EP]
- Davis DR, Weidenschilling SJ, Chapman CR, et al (1984) Saturn ring particles as dynamic ephemeral bodies. *Science* 224(4650):744–747. <https://doi.org/10.1126/science.224.4650.744>
- Dermott SF, Murray CD (1981) The dynamics of tadpole and horseshoe orbits II. The coorbital satellites of Saturn. *Icarus* 48(1):12–22. [https://doi.org/10.1016/0019-1035\(81\)90148-2](https://doi.org/10.1016/0019-1035(81)90148-2)
- Dermott SF, Gold T, Sinclair AT (1979) The rings of Uranus: nature and origin. *Astron J* 84:1225–1232. <https://doi.org/10.1086/112533>
- Dobrovolskis AR (2019) Classification of ellipsoids by shape and surface gravity. *Icarus* 321:891–928. <https://doi.org/10.1016/j.icarus.2018.11.023>
- El Moutamid M, Nicholson PD, French RG, et al (2016) How Janus' orbital swap affects the edge of Saturn's A ring? *Icarus* 279:125–140. <https://doi.org/10.1016/j.icarus.2015.10.025>. arXiv:1510.00434 [astro-ph.EP]
- Esposito LW, Barth CA, Colwell JE, et al (2004) The Cassini ultraviolet imaging spectrograph investigation. *Space Sci Rev* 115(1–4):299–361. <https://doi.org/10.1007/s11214-004-1455-8>
- Filacchione G, Capaccioni F, Clark RN, et al (2010) Saturn's icy satellites investigated by Cassini-VIMS. II. Results at the end of nominal mission. *Icarus* 206(2):507–523. <https://doi.org/10.1016/j.icarus.2009.11.006>
- Filacchione G, Capaccioni F, Ciarniello M, et al (2012) Saturn's icy satellites and rings investigated by Cassini-VIMS: III - radial compositional variability. *Icarus* 220(2):1064–1096. <https://doi.org/10.1016/j.icarus.2012.06.040>. arXiv:1203.6230 [astro-ph.EP]
- Filacchione G, Capaccioni F, Clark RN, et al (2013) The radial distribution of water ice and chromophores across Saturn's system. *Astrophys J* 766(2):76. <https://doi.org/10.1088/0004-637X/766/2/76>. arXiv:1301.6611 [astro-ph.EP]
- Filacchione G, Ciarniello M, Capaccioni F, et al (2014) Cassini-VIMS observations of Saturn's main rings: I. Spectral properties and temperature radial profiles variability with phase angle and elevation. *Icarus* 241:45–65. <https://doi.org/10.1016/j.icarus.2014.06.001>
- Filacchione G, Ciarniello M, D'Aversa E, et al (2022) Saturn's icy satellites investigated by Cassini - VIMS. V. Spectrophotometry. *Icarus* 375:114803. <https://doi.org/10.1016/j.icarus.2021.114803>. arXiv:2111.15541 [astro-ph.EP]

- French RG, McGhee CA, Dones L, et al (2003) Saturn's wayward shepherds: the peregrinations of Prometheus and Pandora. *Icarus* 162(1):143–170. [https://doi.org/10.1016/S0019-1035\(02\)00050-7](https://doi.org/10.1016/S0019-1035(02)00050-7)
- French RG, McGhee-French CA, Loneragan K, et al (2017) Noncircular features in Saturn's rings IV: absolute radius scale and Saturn's pole direction. *Icarus* 290:14–45
- Goldreich P, Rappaport N (2003) Chaotic motions of Prometheus and Pandora. *Icarus* 162(2):391–399. [https://doi.org/10.1016/S0019-1035\(02\)00080-5](https://doi.org/10.1016/S0019-1035(02)00080-5)
- Hapke B (2012) Theory of reflectance and emittance spectroscopy, 2nd edn. Cambridge University Press, Cambridge. <https://doi.org/10.1017/CBO9781139025683>
- Hedman MM, Murray CD, Cooper NJ, et al (2009) Three tenuous rings/arcs for three tiny moons. *Icarus* 199(2):378–386. <https://doi.org/10.1016/j.icarus.2008.11.001>
- Hedman MM, Cooper NJ, Murray CD, et al (2010) Aegaeon (Saturn LIII), a G-ring object. *Icarus* 207(1):433–447. <https://doi.org/10.1016/j.icarus.2009.10.024>. [arXiv:0911.0171](https://arxiv.org/abs/0911.0171) [astro-ph.EP]
- Hedman MM, Nicholson PD, Showalter MR, et al (2011) The Christiansen effect in Saturn's narrow dusty rings and the spectral identification of clumps in the F ring. *Icarus* 215(2):695–711. <https://doi.org/10.1016/j.icarus.2011.02.025>. [arXiv:1102.5116](https://arxiv.org/abs/1102.5116) [astro-ph.EP]
- Hedman MM, Nicholson PD, Cuzzi JN, et al (2013) Connections between spectra and structure in Saturn's main rings based on Cassini VIMS data. *Icarus* 223(1):105–130. <https://doi.org/10.1016/j.icarus.2012.10.014>. [arXiv:1210.4727](https://arxiv.org/abs/1210.4727) [astro-ph.EP]
- Hedman MM, Helfenstein P, Chancia RO, et al (2020) Photometric analyses of Saturn's small moons: Aegaeon, Methone, and Pallene are dark; Helene and Calypso are bright. *Astron J* 159(4):129. <https://doi.org/10.3847/1538-3881/ab659d>. [arXiv:1912.09192](https://arxiv.org/abs/1912.09192) [astro-ph.EP]
- Hendrix AR, Filacchione G, Paranicas C, et al (2018) Icy Saturnian satellites: disk-integrated UV-IR characteristics and links to exogenic processes. *Icarus* 300:103–114. <https://doi.org/10.1016/j.icarus.2017.08.037>
- Hendrix AR, French RG, Buratti BJ, et al (2022) The ultraviolet-visible spectra of Iapetus: unique insights into the composition of the dark material. In: AGU Fall Meeting abstracts, pp P22B–2102
- Holsapple KA, Michel P (2006) Tidal disruptions: a continuum theory for solid bodies. *Icarus* 183(2):331–348. <https://doi.org/10.1016/j.icarus.2006.03.013>
- Hsu HW, Postberg F, Sekine Y, et al (2015) Ongoing hydrothermal activities within Enceladus. *Nature* 519(7542):207–210. <https://doi.org/10.1038/nature14262>
- Imanaka H, Khare BN, Elsila JE, et al (2004) Laboratory experiments of Titan tholin formed in cold plasma at various pressures: implications for nitrogen-containing polycyclic aromatic compounds in Titan haze. *Icarus* 168(2):344–366. <https://doi.org/10.1016/j.icarus.2003.12.014>
- Imanaka H, Cruikshank DP, Khare BN, et al (2012) Optical constants of Titan tholins at mid-infrared wavelengths (2.5–25 μm) and the possible chemical nature of Titan's haze particles. *Icarus* 218(1):247–261. <https://doi.org/10.1016/j.icarus.2011.11.018>
- Jacobson RA (2014) The small saturnian satellites – chaos and conundrum. In: AAS/Division of Dynamical Astronomy Meeting #45, p 304.05
- Jacobson RA (2022) The orbits of the main saturnian satellites, the saturnian system gravity field, and the orientation of Saturn's pole. *Astron J* 164(5):199. <https://doi.org/10.3847/1538-3881/ac90c9>
- Jacobson RA, Spitale J, Porco CC, et al (2008) Revised orbits of Saturn's small inner satellites. *Astron J* 135(1):261–263. <https://doi.org/10.1088/0004-6256/135/1/261>
- Jurac S, Richardson JD (2007) Neutral cloud interaction with Saturn's main rings. *Geophys Res Lett* 34(8):L08102. <https://doi.org/10.1029/2007GL029567>
- Kaasalainen M, Torppa J, Muinonen K (2001) Optimization methods for asteroid lightcurve inversion. II. The complete inverse problem. *Icarus* 153(1):37–51. <https://doi.org/10.1006/icar.2001.6674>
- Kempf S, Altobelli N, Schmidt J, et al (2023) Micrometeoroid infall onto Saturn's rings constrains their age to no more than a few hundred million years. *Sci Adv* 9(19):eadf8537. <https://doi.org/10.1126/sciadv.adf8537>
- Khare BN, Sagan C, Arakawa ET, et al (1984) Optical constants of organic tholins produced in a simulated Titanian atmosphere: from soft X-ray to microwave frequencies. *Icarus* 60(1):127–137. [https://doi.org/10.1016/0019-1035\(84\)90142-8](https://doi.org/10.1016/0019-1035(84)90142-8)
- Khare BN, Sagan C, Thompson WR, et al (1994) Optical properties of poly-HCN and their astronomical applications. *Can J Chem* 72:678–694
- Krimigis SM, Mitchell DG, Hamilton DC, et al (2004) Magnetosphere Imaging Instrument (MIMI) on the Cassini Mission to Saturn/Titan. *Space Sci Rev* 114(1–4):233–329. <https://doi.org/10.1007/s11214-004-1410-8>
- Lainey V, Karatekin Ö, Desmars J, et al (2012) Strong tidal dissipation in Saturn and constraints on Enceladus' thermal state from astrometry. *Astrophys J* 752(1):14. <https://doi.org/10.1088/0004-637X/752/1/14>. [arXiv:1204.0895](https://arxiv.org/abs/1204.0895) [astro-ph.EP]


- Lainey V, Noyelles B, Cooper N, et al (2019) Interior properties of the inner saturnian moons from space astrometry data. *Icarus* 326:48–62. <https://doi.org/10.1016/j.icarus.2019.01.026>. arXiv:1903.03603 [astro-ph.EP]
- Lainey V, Rambaux N, Cooper N, et al (2023) Characterising the interior of five inner saturnian moons using Cassini ISS data. *Astron Astrophys* 670:L25. <https://doi.org/10.1051/0004-6361/202244757>
- Leleu A, Jutzi M, Rubin M (2018) The peculiar shapes of Saturn's small inner moons as evidence of mergers of similar-sized moonlets. *Nat Astron* 2:555–561. <https://doi.org/10.1038/s41550-018-0471-7>. arXiv:1805.08682 [astro-ph.EP]
- Lissauer JJ, Cuzzi JN (1982) Resonances in Saturn's rings. *Astron J* 87:1051–1058. <https://doi.org/10.1086/113189>
- Lissauer JJ, Peale SJ, Cuzzi JN (1984) Ring torque on janus and the melting of Enceladus. *Icarus* 58(2):159–168. [https://doi.org/10.1016/0019-1035\(84\)90034-4](https://doi.org/10.1016/0019-1035(84)90034-4)
- Lissauer JJ, Goldreich P, Tremaine S (1985) Evolution of the Janus-Epimetheus coorbital resonance due to torques from Saturn's ring. *Icarus* 64(3):425–434. [https://doi.org/10.1016/0019-1035\(85\)90066-1](https://doi.org/10.1016/0019-1035(85)90066-1)
- McDonald GD, Thompson WR, Heinrich M, et al (1994) Chemical investigation of Titan and Triton tholins. *Icarus* 108(1):137–145. <https://doi.org/10.1006/icar.1994.1046>
- Miller KE, Filacchione G, Cuzzi JN, et al (2024) The composition of Saturn's Rings. *Space Sci Rev* 220:70. <https://doi.org/10.1007/s11214-024-01104-y>
- Morrison SJ, Thomas PC, Tiscareno MS, et al (2009) Grooves on small saturnian satellites and other objects: characteristics and significance. *Icarus* 204(1):262–270. <https://doi.org/10.1016/j.icarus.2009.06.003>
- Murray CD, French RS (2018) The F ring of Saturn. In: Tiscareno MS, Murray CD (eds) *Planetary ring systems. Properties, structure, and evolution*. Cambridge University Press, Cambridge, pp 338–362. <https://doi.org/10.1017/9781316286791.013>
- Murray CD, Giulianti Winter SM (1996) Periodic collisions between the moon Prometheus and Saturn's F ring. *Nature* 380(6570):139–141. <https://doi.org/10.1038/380139a0>
- Murray CD, Chavez C, Beurle K, et al (2005) How Prometheus creates structure in Saturn's F ring. *Nature* 437(7063):1326–1329. <https://doi.org/10.1038/nature04212>
- Nicholson PD, Hamilton DP, Matthews K, et al (1992) New observations of Saturn's coorbital satellites. *Icarus* 100(2):464–484. [https://doi.org/10.1016/0019-1035\(92\)90111-J](https://doi.org/10.1016/0019-1035(92)90111-J)
- Nicholson PD, Hedman MM, Clark RN, et al (2008) A close look at Saturn's rings with Cassini VIMS. *Icarus* 193(1):182–212. <https://doi.org/10.1016/j.icarus.2007.08.036>
- Nicholson PD, French RG, Spitale JN (2018) Narrow rings, gaps, and sharp edges. In: Tiscareno MS, Murray CD (eds) *Planetary ring systems. Properties, structure, and evolution*. Cambridge University Press, Cambridge, pp 276–307. <https://doi.org/10.1017/9781316286791.011>
- Pang KD, Voge CC, Rhoads JW, et al (1984) The E ring of Saturn and satellite Enceladus. *J Geophys Res* 89:9459–9470. <https://doi.org/10.1029/JB089iB11p09459>
- Paranicas C, Hibbitts C, Kollmann P, et al (2018) Magnetospheric considerations for Solar System ice state. *Icarus* 302:560–564. <https://doi.org/10.1016/j.icarus.2017.12.013>
- Perry M, Cravens T, Smith H, et al (2017) In-situ measurements of ions and neutrals near Saturn's f-ring. In: *European Planetary Science Congress*, pp EPSC2017–951
- Porco CC, West RA, Squyres S, et al (2004) Cassini imaging science: instrument characteristics and anticipated scientific investigations at Saturn. *Space Sci Rev* 115(1–4):363–497. <https://doi.org/10.1007/s11214-004-1456-7>
- Porco CC, Baker E, Barbara J, et al (2005) Cassini imaging science: initial results on Saturn's rings and small satellites. *Science* 307(5713):1226–1236. <https://doi.org/10.1126/science.1108056>
- Porco CC, Thomas PC, Weiss JW, et al (2007) Saturn's small inner satellites: clues to their origins. *Science* 318(5856):1602. <https://doi.org/10.1126/science.1143977>
- Porco CC, Weiss JW, Richardson DC, et al (2008) Simulations of the dynamical and light-scattering behavior of Saturn's rings and the derivation of ring particle and disk properties. *Astron J* 136(5):2172–2200. <https://doi.org/10.1088/0004-6256/136/5/2172>
- Postberg F, Kempf S, Schmidt J, et al (2009) Sodium salts in E-ring ice grains from an ocean below the surface of Enceladus. *Nature* 459(7250):1098–1101. <https://doi.org/10.1038/nature08046>
- Postberg F, Schmidt J, Hillier J, et al (2011) A salt-water reservoir as the source of a compositionally stratified plume on Enceladus. *Nature* 474(7353):620–622. <https://doi.org/10.1038/nature10175>
- Postberg F, Clark RN, Hansen CJ, et al (2018) Plume and surface composition of Enceladus. In: Schenk PM, Clark RN, Howett CJA, et al (eds) *Enceladus and the icy moons of Saturn*. University of Arizona Press, Tucson, p 129. https://doi.org/10.2458/azu_uapress_9780816537075-ch007
- Poulet F, Sicardy B (2001) Dynamical evolution of the Prometheus-Pandora system. *Mon Not R Astron Soc* 322(2):343–355. <https://doi.org/10.1046/j.1365-8711.2001.04128.x>
- Poulet F, Cruikshank DP, Cuzzi JN, et al (2003) Compositions of Saturn's rings A, B, and C from high resolution near-infrared spectroscopic observations. *Astron Astrophys* 412:305–316. <https://doi.org/10.1051/0004-6361:20031123>

- Quillen AC, Zaidouni F, Nakajima M, et al (2021) Accretion of ornamental equatorial ridges on Pan, Atlas and Daphnis. *Icarus* 357:114260. <https://doi.org/10.1016/j.icarus.2020.114260>. arXiv:2007.13227 [astro-ph.EP]
- Rambaux N, Lainey V, Cooper N, et al (2022) Spherical harmonic decomposition and interpretation of the shapes of the small saturnian inner moons. *Astron Astrophys* 667:A78. <https://doi.org/10.1051/0004-6361/202243355>
- Renner S, Cooper NJ, El Moutamid M, et al (2016) Origin of the chaotic motion of the saturnian satellite atlas. *Astron J* 151(5):122. <https://doi.org/10.3847/0004-6256/151/5/122>. arXiv:1602.01967 [astro-ph.EP]
- Roberts JH, Barnouin OS, Daly MG, et al (2021) Rotational states and shapes of Ryugu and Bennu: implications for interior structure and strength. *Planet Space Sci* 204:105268. <https://doi.org/10.1016/j.pss.2021.105268>
- Roche E (1851) La figure d'une masse fluide, soumise à l'attraction d'un point éloigné. *Mem Acad Sci Montpellier* 1:20
- Rousses E, Krupp N, Armstrong TP, et al (2008) Discovery of a transient radiation belt at Saturn. *Geophys Res Lett* 35(22). <https://doi.org/10.1029/2008GL035767>
- Salmon J, Charnoz S, Crida A, et al (2010) Long-term and large-scale viscous evolution of dense planetary rings. *Icarus* 209(2):771–785. <https://doi.org/10.1016/j.icarus.2010.05.030>. arXiv:1006.0633 [astro-ph.EP]
- Santana T, Tajeddine R, El Moutamid M, et al (2019) Daphnis' chaotic orbit. In: EPSC-DPS joint meeting 2019, pp EPSC-DPS2019–1085
- Sheppard SS, Tholen DJ, Alexandersen M, et al (2023) New Jupiter and Saturn satellites reveal new moon dynamical families. *Res Notes AAS* 7(5):100. <https://doi.org/10.3847/2515-5172/acd766>
- Shkuratov Y, Starukhina L, Hoffmann H, et al (1999) A model of spectral albedo of particulate surfaces: implications for optical properties of the Moon. *Icarus* 137(2):235–246. <https://doi.org/10.1006/icar.1998.6035>
- Shkuratov YG, Stankevich DG, Petrov DV, et al (2005) Interpreting photometry of regolith-like surfaces with different topographies: shadowing and multiple scattering. *Icarus* 173(1):3–15. <https://doi.org/10.1016/j.icarus.2003.12.017>
- Shkuratov Y, Kaydash V, Korokhin V, et al (2011) Optical measurements of the Moon as a tool to study its surface. *Planet Space Sci* 59(13):1326–1371. <https://doi.org/10.1016/j.pss.2011.06.011>
- Shkuratov Y, Kaydash V, Korokhin V, et al (2012) A critical assessment of the Hapke photometric model. *J Quant Spectrosc Radiat Transf* 113(18):2431–2456. <https://doi.org/10.1016/j.jqsrt.2012.04.010>
- Showalter MR, Cuzzi JN, Marouf EA, et al (1986) Satellite “wakes” and the orbit of the Encke gap moonlet. *Icarus* 66(2):297–323. [https://doi.org/10.1016/0019-1035\(86\)90160-0](https://doi.org/10.1016/0019-1035(86)90160-0)
- Spahn F, Hoffmann H, Rein H, et al (2018) Moonlets in dense planetary rings. In: Tiscareno MS, Murray CD (eds) *Planetary ring systems. Properties, structure, and evolution*, pp 157–197. <https://doi.org/10.1017/9781316286791.008>
- Spitale JN, Porco CC (2009) Time variability in the outer edge of Saturn's A-ring revealed by Cassini imaging. *Astron J* 138(5):1520–1528. <https://doi.org/10.1088/0004-6256/138/5/1520>
- Spitale JN, Jacobson RA, Porco CC, et al (2006) The orbits of Saturn's small satellites derived from combined historic and Cassini imaging observations. *Astron J* 132(2):692–710. <https://doi.org/10.1086/505206>
- Srama R, Ahrens TJ, Altobelli N, et al (2004) The Cassini cosmic dust analyzer. *Space Sci Rev* 114(1–4):465–518. <https://doi.org/10.1007/s11214-004-1435-z>
- Stephan K, Ciarniello M, Poch O, et al (2021) VIS-NIR/SWIR spectral properties of H₂O ice depending on particle size and surface temperature. *Minerals* 11(12):1328. <https://doi.org/10.3390/min11121328>
- Tajeddine R, Nicholson PD, Longaretti PY, et al (2017a) What confines the rings of Saturn? *Astrophys J Suppl Ser* 232(2):28. <https://doi.org/10.3847/1538-4365/aa8c09>. arXiv:1710.08462 [astro-ph.EP]
- Tajeddine R, Nicholson PD, Tiscareno MS, et al (2017b) Dynamical phenomena at the inner edge of the Keeler gap. *Icarus* 289:80–93. <https://doi.org/10.1016/j.icarus.2017.02.002>. arXiv:1709.01974 [astro-ph.EP]
- Thomas PC (2010) Sizes, shapes, and derived properties of the saturnian satellites after the Cassini nominal mission. *Icarus* 208(1):395–401. <https://doi.org/10.1016/j.icarus.2010.01.025>
- Thomas P, Helfenstein P (2020) The small inner satellites of Saturn: shapes, structures and some implications. *Icarus* 344:113355. <https://doi.org/10.1016/j.icarus.2019.06.016>
- Thomas PC, Armstrong JW, Asmar SW, et al (2007) Hyperion's sponge-like appearance. *Nature* 448(7149):50–56. <https://doi.org/10.1038/nature05779>
- Thomas PC, Burns JA, Hedman M, et al (2013) The inner small satellites of Saturn: a variety of worlds. *Icarus* 226(1):999–1019. <https://doi.org/10.1016/j.icarus.2013.07.022>
- Thomas P, Joseph J, Ansty T (2018a) Saturn Small Moon Shape Models Bundle V1.0. NASA Planetary Data System, p. 3. <https://doi.org/10.26033/ewy3-jy61>

- Thomas PC, Tiscareno MS, Helfenstein P (2018b) The inner small satellites of Saturn, and hyperion. In: Schenk PM, Clark RN, Howett CJA, et al (eds) Enceladus and the icy moons of Saturn. University of Arizona Press, Tucson, p 387. https://doi.org/10.2458/azu_uapress_9780816537075-ch019
- Tiscareno MS, Burns JA, Nicholson PD, et al (2007) Cassini imaging of Saturn's rings. II. A wavelet technique for analysis of density waves and other radial structure in the rings. *Icarus* 189(1):14–34. <https://doi.org/10.1016/j.icarus.2006.12.025>. arXiv:astro-ph/0610242 [astro-ph]
- Tiscareno MS, Burns JA, Hedman MM, et al (2008) The population of propellers in Saturn's A ring. *Astron J* 135(3):1083–1091. <https://doi.org/10.1088/0004-6256/135/3/1083>. arXiv:0710.4547 [astro-ph]
- Tiscareno MS, Thomas PC, Burns JA (2009) The rotation of Janus and Epimetheus. *Icarus* 204(1):254–261. <https://doi.org/10.1016/j.icarus.2009.06.023>. arXiv:0904.3515 [astro-ph]
- Tseng WL, Ip WH (2011) An assessment and test of Enceladus as an important source of Saturn's ring atmosphere and ionosphere. *Icarus* 212(1):294–299. <https://doi.org/10.1016/j.icarus.2010.12.003>
- Tseng WL, Ip WH, Johnson RE, et al (2010) The structure and time variability of the ring atmosphere and ionosphere. *Icarus* 206(2):382–389. <https://doi.org/10.1016/j.icarus.2009.05.019>
- Tseng WL, Johnson RE, Thomsen MF, et al (2011) Neutral H₂ and H₂⁺ ions in the saturnian magnetosphere. *J Geophys Res Space Phys* 116(A3):A03209. <https://doi.org/10.1029/2010JA016145>
- Vahidinia S, Cuzzi JN, Hedman M, et al (2011) Saturn's F ring grains: aggregates made of crystalline water ice. *Icarus* 215(2):682–694. <https://doi.org/10.1016/j.icarus.2011.04.011>
- Verbiscer A, French R, Showalter M, et al (2007) Enceladus: cosmic graffiti artist caught in the act. *Science* 315(5813):815. <https://doi.org/10.1126/science.1134681>
- Veverka J (1971) The meaning of Russell's law. *Icarus* 14(2):284–285. [https://doi.org/10.1016/0019-1035\(71\)90066-2](https://doi.org/10.1016/0019-1035(71)90066-2)
- Waite JH, Lewis WS, Kasprzak WT, et al (2004) The Cassini Ion and Neutral Mass Spectrometer (INMS) investigation. *Space Sci Rev* 114(1–4):113–231. <https://doi.org/10.1007/s11214-004-1408-2>
- Walker JD, Chocron S, Waite JH, et al (2015) The vaporization threshold: hypervelocity impacts of ice grains into a titanium Cassini spacecraft instrument chamber. *Proc Eng* 103:628–635
- Weidenschilling SJ, Chapman CR, Davis DR, et al (1984) Ring particles: collisional interactions and physical nature. In: Greenberg R, Brahic A (eds) Planetary rings. University of Arizona Press, Tucson, pp 367–415. <https://doi.org/10.1017/9781316286791.010>
- Weiss JW, Porco CC, Tiscareno MS (2009) Ring edge waves and the masses of nearby satellites. *Astron J* 138(1):272–286. <https://doi.org/10.1088/0004-6256/138/1/272>
- West R, Lavvas P, Anderson C, et al (2014) Titan's haze. In: Titan, p 285. <https://doi.org/10.1017/CBO9780511667398.011>
- Yoder CF, Synnott SP, Salo H (1989) Orbits and masses of Saturn's co-orbiting satellites, Janus and Epimetheus. *Astron J* 98:1875. <https://doi.org/10.1086/115265>

Publisher's Note Springer Nature remains neutral with regard to jurisdictional claims in published maps and institutional affiliations.

Authors and Affiliations

Mauro Ciarniello¹  · Gianrico Filacchione¹ · Philip D. Nicholson² · Matthew M. Hedman³ · Sebastien Charnoz⁴ · Jeffrey N. Cuzzi⁵ · Maryame El Moutamid⁶ · Amanda R. Hendrix⁷ · Nicolas Rambaux⁸ · Kelly E. Miller⁹ · Olivier Mousis^{10,11} · Kevin Baillie⁸ · Paul R. Estrada⁵ · J. Hunter Waite⁹

✉ M. Ciarniello
mauro.ciarniello@inaf.it

G. Filacchione
gianrico.filacchione@inaf.it

P.D. Nicholson
pdn2@cornell.edu

M.M. Hedman
mhedman@uidaho.edu

S. Charnoz
charnoz@ipgp.fr

J.N. Cuzzi
jeffrey.cuzzi@nasa.gov

M. El Moutamid
maryame.elmoutamid@swri.org

A.R. Hendrix
ahendrix@psi.edu

N. Rambaux
nicolas.rambaux@obspm.fr

K.E. Miller
kelly.miller@swri.org

O. Mousis
olivier.mousis@lam.fr

K. Baillié
kevin.baillie@obspm.fr

P.R. Estrada
paul.r.estrada@nasa.gov

J.H. Waite
hunterwaite@gmail.com

- ¹ Istituto di Astrofisica e Planetologia Spaziali, Istituto Nazionale di Astrofisica, via del Fosso del Cavaliere, 100, Rome, 00133, Italy
- ² Astronomy Department, Cornell University, Ithaca, 14853, NY, USA
- ³ Department of Physics and Astronomy, University of Idaho, Moscow, 83844, ID, USA
- ⁴ Université Paris Cité, Institut de Physique du Globe de Paris, CNRS, Paris F-75005, France
- ⁵ Space Sciences Division, NASA Ames Research Center, MS 245-3, Moffett Field, 94035, CA, USA
- ⁶ Southwest Research Institute, Boulder, CO, USA
- ⁷ Planetary Science Institute, Tucson, AZ, USA
- ⁸ IMCCE, Observatoire de Paris, PSL University, CNRS, Sorbonne Université, Paris, 77 Avenue Denfert-Rochereau, Paris, 75014, France
- ⁹ Southwest Research Institute, San Antonio, TX, USA
- ¹⁰ Aix-Marseille Université, CNRS, CNES, Institut Origines, LAM, Marseille, France
- ¹¹ Institut universitaire de France (IUF), Paris, France